J. Fluid Mech. (2013), *vol.* 733, *pp.* 473–503. © Cambridge University Press 2013
doi:10.1017/jfm.2013.426

Optimal mode decomposition for unsteady flows

A. Wynn[1,†], D. S. Pearson[1], B. Ganapathisubramani[1,2] and P. J. Goulart[1,3]

[1]Department of Aeronautics, Imperial College London, London SW7 2AZ, UK

[2]Aerodynamics and Flight Mechanics Group, University of Southampton, Southampton SO17 1BJ, UK

[3]Automatic Control Laboratory, ETH Zürich, 8092 Zurich, Switzerland

(Received 25 June 2012; revised 30 April 2013; accepted 10 August 2013;
first published online 24 September 2013)

A new method, herein referred to as optimal mode decomposition (OMD), of finding a linear model to describe the evolution of a fluid flow is presented. The method estimates the linear dynamics of a high-dimensional system which is first projected onto a subspace of a user-defined fixed rank. An iterative procedure is used to find the optimal combination of linear model and subspace that minimizes the system residual error. The OMD method is shown to be a generalization of dynamic mode decomposition (DMD), in which the subspace is not optimized but rather fixed to be the proper orthogonal decomposition (POD) modes. Furthermore, OMD is shown to provide an approximation to the Koopman modes and eigenvalues of the underlying system. A comparison between OMD and DMD is made using both a synthetic waveform and an experimental data set. The OMD technique is shown to have lower residual errors than DMD and is shown on a synthetic waveform to provide more accurate estimates of the system eigenvalues. This new method can be used with experimental and numerical data to calculate the 'optimal' low-order model with a user-defined rank that best captures the system dynamics of unsteady and turbulent flows.

Key words: computational methods, low-dimensional models, nonlinear dynamical systems

1. Introduction

The temporal dynamics of a fluid flow form an infinite-dimensional system. A common objective is to find a low-order representation of the fluid system which is amenable to estimation and control methods. The reasons for wanting to control the motion of a fluid are many and varied, such as reducing drag, noise, vibration or to promote efficient mixing. Often, in practical applications, the economic argument for even the most modest improvement in these areas is compelling. Therefore, the question of how best to approximate high-dimensional dynamics by a lower-dimensional system is a pertinent one. In many instances, even defining what constitutes the *best* estimate is not obvious and is dependent on the task at hand.

In some instances the dominant features of the flow, such as regular vortex shedding or a steady separation point, can be modelled using analytic expressions with appropriate approximations and used in control schemes. These methods are successful when carefully applied (Pastoor *et al.* 2008), but they lack the general

† Email address for correspondence: a.wynn@imperial.ac.uk

https://doi.org/10.1017/jfm.2013.426 Published online by Cambridge University Press

applicability offered by a data-driven approach. In these approaches, large sets of data from experiment or simulation are acquired with the objective of consolidating it into some reduced form, while retaining the most important dynamic information.

The first notable progress toward this goal was made by Lumley (1970) and Sirovich (1987) with the introduction of proper orthogonal decomposition (POD), sometimes also called Karhunen–Loève decomposition. This method decomposes the given data set into a set of weighted orthogonal basis functions, or modes, which are ordered according to the magnitude of their singular values and truncated as required. This is equivalent to retaining the modes that capture the maximum proportion of the flow energy for a given order of system. The POD modes do not contain any information on the system dynamics, but provide a reduced-order representation of the flow which can be subsequently used in methods such as Galerkin projection. It has been used with notable success in the description of flows with dominant or periodic features such as jets, wakes, etc. to identify coherent structures (see Bonnet *et al.* (1994) among various others). The attractiveness of the POD method is its unambiguous mode-selection criteria, ease of calculation and broad applicability. Problems can arise, however, if the flow contains low-energy features that have a disproportionately large influence on system dynamics, as discussed in Noack *et al.* (2003). Such nonlinearities are commonly found in fluid systems, particularly those with high acoustic emissions or with transient growth (Ilak & Rowley 2008). In a POD analysis such features would not be prioritized and may be discarded unwittingly during the truncation of modes (Ma, Ahuja & Rowley 2011), leading to a poor dynamic model. Noack *et al.* (2003) proposed an improvement to POD-based Galerkin models by introducing the concept of a *shift mode*. The shift mode augments the chosen POD basis with a new orthogonal mode representing a correction to the mean flow field. Low-order models created by Galerkin projection using this extended basis can more accurately represent the transient system dynamics (Tadmor *et al.* 2007).

An alternative extension of POD was proposed by Rowley (2005) in the context of snapshot data sampled from a controlled system. The method, known as balanced POD, and involves truncating the set of POD modes in a way that equally prioritizes the observability and controllability of the reduced-order system. Balanced POD has the advantage of preserving modes most relevant to subsequent control analyses as well as providing known error bounds with respect to the truncation. Ma *et al.* (2011) demonstrated that balanced POD produces the same reduced-order system as the eigenvalue realization algorithm (ERA) method devised by Juang & Pappa (1985). Although equivalent, the implementation of each method raises different practical considerations. Balanced POD, unlike ERA, explicitly calculates the truncated system modes, which often prove useful for visual interpretation of the fluid model. However, ERA does not require adjoint information so, unlike balanced POD, is not restricted to use only on numerical simulations. A detailed comparison of balanced POD and the ERA is provided by Ma *et al.* (2011).

Schmid (2010, 2011) recognized that the modes of a reduced-order system can be given a dynamic context by inspecting the eigenvalues of a matrix approximating their evolution. This approach, called dynamic mode decomposition (DMD), was also shown by Rowley *et al.* (2009) to fit within a more general framework of analysis utilizing the Koopman operator. Schmid (2010) arranged the data into a time-ordered set and projected it onto a truncated POD basis in order to make the problem numerically tractable. The eigenvalues of the resulting linear model can then be directly related to the POD modes on which the model is based. This provides each mode with an interpretation in terms of its decay rate and frequency content. Applying

https://doi.org/10.1017/jfm.2013.426 Published online by Cambridge University Press

DMD to both experimental and numerical test data, Schmid (2010, 2011) found that the eigenvalues of the linear map form groups and patterns in which the corresponding modes have similar structural features.

The present study demonstrates that choosing the truncated set of POD modes as the basis of the DMD analysis restricts its performance. One reason for this is that POD modes do not intrinsically contain any dynamical information about the flow. In this paper, a more general solution is proposed in which the low-rank basis and linear dynamic matrix are calculated simultaneously. In this way, dynamical information is utilized in the construction of the mode shapes which form the low-rank basis. By doing this, an optimum can be found for which the residual error of the linear approximation to the system evolution is always the same or smaller than that of DMD.

The new method, called optimal mode decomposition (OMD), is formulated in § 2 with an explanation of how it generalizes DMD as a linear modelling methodology. Alternatively, DMD may be interpreted (Rowley *et al.* 2009) as a method of approximating the Koopman modes of the underlying fluid system (see Bagheri (2013) for a discussion of when this interpretation is appropriate). Consequently, in § 3 we discuss DMD, OMD and a recently developed technique 'optimized dynamic mode decomposition' (opt-DMD) (Chen, Tu & Rowley 2012) in this context. It is shown that the OMD algorithm can be thought of as providing a low-order approximation to the action of the Koopman operator on the observable (see § 3 for the definition of an *observable*) describing the data measurement process. OMD is also a natural generalization of DMD in this context. However, it is explained why, at the current state of the literature, it is unclear which method provides the best approximation to the Koopman modes and eigenvalues. An algorithm for solving the OMD optimization problem is proposed in § 4, followed by demonstrations on both synthetic and experimental data set in §§ 5 and 6, respectively.

2. Low-order modelling, DMD and OMD

Suppose that $f(\boldsymbol{x}, t)$ represents the velocity of a fluid flow at time t and spatial location $\boldsymbol{x} \in \Omega$ in the domain $\Omega \subset \mathbb{R}^3$ of the flow. Our aim is to extract information about the dynamics of f from an ensemble of numerical or experimental snapshot data. We assume that N pairs $(\boldsymbol{u}_k, \boldsymbol{u}_k^+)_{k=1}^N$ of velocity snapshots are available. The vector $\boldsymbol{u}_k$ contains velocity data over a given field of view $\{\boldsymbol{x}_1, \ldots, \boldsymbol{x}_p\} \subset \Omega$ at time t_k, while $\boldsymbol{u}_k^+$ is a snapshot recorded after some fixed time interval Δt. The snapshot data can therefore be written as

$$\boldsymbol{u}_k = \begin{bmatrix} f(\boldsymbol{x}_1, t_k) \\ \vdots \\ f(\boldsymbol{x}_p, t_k) \end{bmatrix} \in \mathbb{R}^p, \quad \boldsymbol{u}_k^+ := \begin{bmatrix} f(\boldsymbol{x}_1, t_k + \Delta t) \\ \vdots \\ f(\boldsymbol{x}_p, t_k + \Delta t) \end{bmatrix} \in \mathbb{R}^p. \tag{2.1}$$

It is important to note that, in practice, the function f is *not known* and is *not linear*. The only data available are the snapshots $(\boldsymbol{u}_k, \boldsymbol{u}_k^+)$ which must be used to deduce information about the underlying process $f(\boldsymbol{x}, t)$. Note also that it is not assumed that the data is sequential, i.e. $t_{k+1} \neq t_k + \Delta t$ in general. To extract dynamical information from (2.1), we aim to construct an approximation to the linearized dynamics of f over the time step Δt. That is, we search for a matrix $\boldsymbol{X} \in \mathbb{R}^{p \times p}$ such that $\boldsymbol{X}\boldsymbol{u}_i \approx \boldsymbol{u}_i^+$ for each snapshot pair $(\boldsymbol{u}_i, \boldsymbol{u}_i^+)$. Each candidate $\boldsymbol{X}$ for the linearized dynamics has an associated

https://doi.org/10.1017/jfm.2013.426 Published online by Cambridge University Press

set of residual vectors $\boldsymbol{r}_i$ satisfying

$$\boldsymbol{X}\boldsymbol{u}_i = \boldsymbol{u}_i^+ + \boldsymbol{r}_i, \tag{2.2}$$

which appear as a consequence of any system nonlinearities, measurement noise or model inaccuracies. An obvious initial choice for $\boldsymbol{X}$ is the matrix that minimizes the residuals $\boldsymbol{r}_i$, found by solving the minimization problem

$$\min_{\boldsymbol{X}} \|\boldsymbol{A} - \boldsymbol{X}\boldsymbol{B}\|^2 = \min_{\boldsymbol{X}} \sum_{i=1}^{N} \|\boldsymbol{u}_i^+ - \boldsymbol{X}\boldsymbol{u}_i\|_2^2, \tag{2.3}$$

where $\boldsymbol{B} \in \mathbb{R}^{p\times N}$ and $\boldsymbol{A} \in \mathbb{R}^{p\times N}$ are matrices containing the 'before' and 'after' snapshot images:

$$\boldsymbol{B} := (\boldsymbol{u}_1 \mid \cdots \mid \boldsymbol{u}_N), \quad \boldsymbol{A} := \left(\boldsymbol{u}_1^+ \mid \cdots \mid \boldsymbol{u}_N^+\right). \tag{2.4}$$

In (2.3) and for the remainder of the paper, $\|\cdot\|$ denotes the Frobenius matrix norm.

The drawback of this approach is that each snapshot $\boldsymbol{u}_k \in \mathbb{R}^p$ contains velocity information at every point of the chosen spatial domain, meaning that p is typically very large. Therefore, $\boldsymbol{X} \in \mathbb{R}^{p\times p}$ with $p \gg N$ and solving (2.3) necessarily results in an overfit of the data. The aim of low-order flow modelling is to overcome this problem by constructing a *low-rank* matrix $\boldsymbol{X}$ from which fundamental properties of the flow can be deduced.

In § 2.2 we describe how such a matrix $\boldsymbol{X}$ may be constructed by solving a rank-constrained version of (2.3), providing a low-order approximation of the flow in terms of intrinsic mode shapes and associated linearized dynamics. It is shown that the resulting optimization problem reduces, in a special case, to the recently developed technique of DMD (Schmid 2010, 2011) and hence provides an extension to DMD. Moreover, numerical experiments in § 5 show that the method developed in this paper more accurately extracts eigenvalue information from snapshot data. We begin by briefly discussing the existing DMD theory.

2.1. *DMD*

In DMD, (2.3) is approximated by solving the associated minimization

$$\min_{\boldsymbol{S}} \|\boldsymbol{A} - \boldsymbol{B}\boldsymbol{S}\|^2 \tag{2.5}$$

where $\boldsymbol{S} \in \mathbb{R}^{N\times N}$, which reduces the problem dimension. Furthermore, the data is assumed to be sequential in the sense that $\boldsymbol{u}_i^+ = \boldsymbol{u}_{i+1}$ and the matrix variable $\boldsymbol{S}$ is assumed to be of companion form (see e.g. Schmid 2010). The reasoning behind this approach is that the DMD method is able to extract eigenvalue information in the case that the underlying dynamics are noise-free and linear. To see why this is true, suppose that the system dynamics satisfy

$$\frac{\partial f}{\partial t} = \boldsymbol{X} f(\boldsymbol{x}, t), \quad t \geqslant 0, \tag{2.6}$$

for a matrix $\boldsymbol{X} \in \mathbb{R}^{p\times p}$ with $\mathrm{rank}(\boldsymbol{X}) \leqslant N$. It follows from (2.1) that

$$\boldsymbol{A} = \mathrm{e}^{\boldsymbol{X}\Delta t}\boldsymbol{B} \tag{2.7}$$

and, consequently, the non-zero eigenvalues of $\boldsymbol{S}$ are equal to the eigenvalues of $\mathrm{e}^{\boldsymbol{X}\Delta t}$ (a proof of this statement is given in appendix A). The *DMD eigenvalues* of the

https://doi.org/10.1017/jfm.2013.426 Published online by Cambridge University Press

system are defined by

$$\lambda_i^{DMD} := \frac{\log \lambda_i(\boldsymbol{S})}{\Delta t}, \tag{2.8}$$

where $\lambda_i(\boldsymbol{S})$ are the eigenvalues of $\boldsymbol{S}$. Hence, it follows that λ_i^{DMD} are exactly the eigenvalues of the true system matrix $\boldsymbol{X}$. In the noise-free linear case, DMD therefore provides a complete dynamical description of the data ensemble. If data is sampled from an underlying system with nonlinear dynamics, then the DMD eigenvalues λ_i^{DMD} instead approximate the system's Koopman modes (Rowley *et al.* 2009). This interpretation is discussed in § 3.

To improve numerical stability, Schmid (2010) showed that one can instead calculate λ_i^{DMD} by using eigenvalues of the matrix $\tilde{\boldsymbol{S}} := \boldsymbol{U}^\top \boldsymbol{A}\boldsymbol{V}\Sigma^{-1}$, where $\boldsymbol{B} = \boldsymbol{U}\Sigma\boldsymbol{V}^\top$ is the compact singular value decomposition of B. This is since the optimal $\boldsymbol{S}$ from (2.5) and $\tilde{S}$ are related by the similarity transformation

$$\tilde{\boldsymbol{S}} = \left(\Sigma \boldsymbol{V}^\top\right) \boldsymbol{S} \left(\boldsymbol{V}\Sigma^{-1}\right). \tag{2.9}$$

Associated with each eigenvalue λ_i^{DMD} is a *dynamic mode*

$$\Phi_i^{DMD} := \boldsymbol{U}\boldsymbol{y}_i \tag{2.10}$$

defined in terms of the eigenvector $\boldsymbol{y}_i$ satisfying $\tilde{\boldsymbol{S}}\boldsymbol{y}_i = \lambda_i(\tilde{\boldsymbol{S}})\boldsymbol{y}_i$. Each mode Φ_i^{DMD} identifies a structure of the flow whose temporal growth rate and frequency are determined by λ_i^{DMD}.

It is shown in this paper that DMD can in fact be directly related to a rank-constrained version of the minimization (2.3), and can therefore be considered as a special case of a more general approach to low-order systems modelling. By appropriately constraining the form of the linear model, a solution can be found that is optimal in the sense of minimizing the norm of the residual error of the system at a chosen rank. This optimization approach will now be introduced before its link to DMD is explained in § 2.4.

2.2. *Low-order modelling via OMD*

To create a low-order approximation of the flow dynamics, we propose to solve the following rank-constrained version of (2.3):

$$\begin{aligned} \min \quad & \|\boldsymbol{A} - \boldsymbol{L}\boldsymbol{M}\boldsymbol{L}^\top \boldsymbol{B}\|^2 \\ \text{s.t.} \quad & \boldsymbol{L}^\top \boldsymbol{L} = \boldsymbol{I} \\ & \boldsymbol{M} \in \mathbb{R}^{r\times r}, \quad \boldsymbol{L} \in \mathbb{R}^{p\times r} \end{aligned} \tag{2.11}$$

where $r = \operatorname{rank}(\boldsymbol{L}\boldsymbol{M}\boldsymbol{L}^\top) \ll p$ is the chosen fixed dimension of the low-order model to be calculated.

In contrast to (2.3) and the DMD approach, (2.11) has two optimization variables, the matrices $\boldsymbol{L}$ and $\boldsymbol{M}$, endowing the low-order approximation with a particular structure, illustrated schematically in figure 1. The matrix $\boldsymbol{L}$ determines a low-dimensional subspace $\mathscr{S}$ of the flow field given by $\mathscr{S} := \operatorname{Im}(\boldsymbol{L}) \subset \mathbb{R}^p$, while M provides dynamics on this low-order subspace. Note that we do not simply solve (2.3) with the pure rank constraint $\operatorname{rank}(\boldsymbol{X}) \leqslant r$, since this would provide no meaningful low-order basis for the flow.

https://doi.org/10.1017/jfm.2013.426 Published online by Cambridge University Press

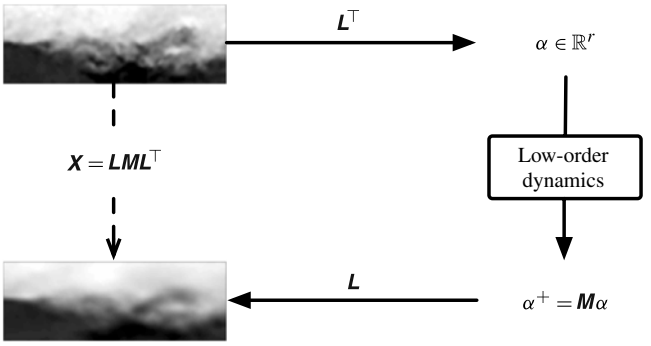


FIGURE 1. Structure of the rank-constrained solution to (2.11). The approximate dynamics $\boldsymbol{X}$ consist of: (i) a projection into $\mathbb{R}^r$ by $\boldsymbol{L}^\top$; (ii) a time-shift by $\boldsymbol{M}$; and (iii) an image reconstruction by $\boldsymbol{L}$.

We now describe, in terms of these two structural components, the evolution

$$\boldsymbol{v} \overset{\boldsymbol{LML}^\top}{\longmapsto} \boldsymbol{v}^+ \tag{2.12}$$

of a flow field $\boldsymbol{v} \in \mathbb{R}^p$ to a flow field $\boldsymbol{v}^+ \in \mathbb{R}^p$ under the low-order dynamics $\boldsymbol{X} = \boldsymbol{LML}^\top$.

The dynamics $\boldsymbol{X} = \boldsymbol{LML}^\top$ has three components, illustrated in figure 1. First, the initial flow field $\boldsymbol{v}$ is represented in the low-dimensional subspace $\mathscr{S}$ by the vector $\boldsymbol{\alpha} = (\alpha_i) = \boldsymbol{L}^\top \boldsymbol{v} \in \mathbb{R}^r$. This vector is a sequence of weights which represent the projection of $\boldsymbol{v}$ into $\mathscr{S}$ by

$$\boldsymbol{P}_{\mathbb{R}^p \to \mathscr{S}}(\boldsymbol{v}) = \sum_{i=1}^{r} \alpha_i \boldsymbol{L}_i, \tag{2.13}$$

where $\boldsymbol{L}_i$ are the columns of $\boldsymbol{L}$. Second, the low-order dynamics of the flow over Δt are governed by $\boldsymbol{M}$ acting on the weight sequence $\boldsymbol{\alpha}$, meaning that the weights of $\boldsymbol{v}^+$ are given by $\boldsymbol{\alpha}^+ := \boldsymbol{M}\boldsymbol{\alpha}$. That is, $\boldsymbol{M}$ is a linear approximation to the evolution of the projection weights, rather than the evolution of the original field $\boldsymbol{v}$. Finally, the flow field $\boldsymbol{v}^+$ is reconstructed by lifting the weight sequence $\boldsymbol{\alpha}^+$ back to the high-dimensional space $\mathbb{R}^p$ via

$$\boldsymbol{v}^+ := \sum_{i=1}^{r} \alpha_i^+ \boldsymbol{L}_i = \boldsymbol{L}\boldsymbol{\alpha}^+. \tag{2.14}$$

Combining the three steps gives $\boldsymbol{v}^+ = \boldsymbol{LML}^\top \boldsymbol{v}$.

The columns of $\boldsymbol{L}$ now have the important interpretation as intrinsic mode shapes of the flow since, by (2.14), the dynamics of the low-order model evolve entirely on $\mathscr{S} = \mathrm{Im}(\boldsymbol{L})$. Note also that due to the constraint $\boldsymbol{L}^\top \boldsymbol{L} = \boldsymbol{I}$, the columns of $\boldsymbol{L}$ are in fact an orthonormal basis for the low-dimensional subspace $\mathscr{S} \subset \mathbb{R}^p$. Hence, $\boldsymbol{L}$ is optimal in the sense that it represents the best r-dimensional subspace of the flow field in which to describe the dynamics of the snapshot data using a linear model. Therefore, we refer to this rank-constrained decomposition as optimal mode decomposition (OMD).

https://doi.org/10.1017/jfm.2013.426 Published online by Cambridge University Press

We now introduce eigenvalues and dynamic modes, analogous to λ_i^{DMD} and Φ_i^{DMD}, associated with the OMD approach (2.11). The OMD eigenvalues are defined by

$$\lambda_i^{OMD} := \frac{\log \lambda_i(\boldsymbol{M})}{\Delta t}, \tag{2.15}$$

where $\lambda_i(\boldsymbol{M})$ are the eigenvalues of low-order dynamics matrix $\boldsymbol{M}$ from (2.11). Associated with each eigenvalue λ_i^{OMD} is a dynamic mode

$$\Phi_i^{OMD} := \boldsymbol{L}z_i \tag{2.16}$$

defined in terms of the eigenvector z_i satisfying $\boldsymbol{M}z_i = \lambda_i(\boldsymbol{M})z_i$ and the low-order subspace basis $\boldsymbol{L}$ from (2.11).

Each mode Φ_i^{OMD} represents a structure of the flow with temporal growth rate $\mathrm{Re}(\lambda_i^{OMD})$ and frequency $\mathrm{Im}(\lambda_i^{OMD})$. To see why this is the case, note that if $\boldsymbol{T}$ is the matrix whose columns are the eigenvectors z_i and Λ is a diagonal matrix containing the eigenvalues $\lambda_i(\boldsymbol{M})$, then

$$\boldsymbol{L}\boldsymbol{M}\boldsymbol{L}^{\top} = \boldsymbol{L}(\boldsymbol{T}\Lambda\boldsymbol{T}^{-1})\boldsymbol{L}^{\top} = (\boldsymbol{L}\boldsymbol{T})\,\Lambda\left(\boldsymbol{T}^{-1}\boldsymbol{L}^{\top}\right). \tag{2.17}$$

Consequently, the modes Φ_i^{OMD} (the columns of $\boldsymbol{L}\boldsymbol{T}$) have temporal growth rate and frequency determined by the eigenvalues λ_i^{OMD}.

Before providing a relationship between $(\lambda_i^{OMD}, \Phi_i^{OMD})$ and their DMD counterparts in § 2.4, we first emphasize the structure inherent in (2.11) by considering the problem of extracting dynamic information from a simple sinusoidal flow.

2.3. *Example: mode shapes and dynamics for a sinusoidal flow*

In this section, it is shown that the dynamics of the sinusoidal flow

$$f(x,t) = \sin(2\pi x - \omega t)\mathrm{e}^{\gamma t} \tag{2.18}$$

can be represented naturally by a model of the form $\boldsymbol{X} = \boldsymbol{L}\boldsymbol{M}\boldsymbol{L}^{\top}$, motivating the OMD method (2.11). Furthermore, the eigenvalues associated with the OMD method are shown to be $\lambda_i^{OMD} = \gamma \pm i\omega$, meaning that the temporal dynamics of the flow can be exactly identified by solving (2.11).

Assume that data is sampled from (2.18) over a spatial window $0 = x_1 < x_2 < \cdots < x_p = 1$ of p equally spaced points in $[0,1]$. For a chosen time step Δt, N pairs $(\boldsymbol{u}_i, \boldsymbol{u}_i^{+})_{i=1}^{N}$ of flow snapshots are recorded in the form (2.1). For this simple example, the two components $\boldsymbol{L}$ and $\boldsymbol{M}$ of the low-order model can be constructed explicitly.

(i) *Low-dimensional subspace basis* $\boldsymbol{L}$*:* the flow dynamics can be separated into spatial mode shapes and temporal weighting functions as

$$f(x,t) = a_1(t)\phi_2(x) + a_2(t)\phi_2(x) \tag{2.19}$$

where $a_1(t) := -\sin(\omega t)\mathrm{e}^{\gamma t}$, $a_2(t) := \cos(\omega t)\mathrm{e}^{\gamma t}$ and $\phi_1(x) := \cos(2\pi x)$, $\phi_2(x) := \sin(2\pi x)$. The snapshots $\boldsymbol{u}_i, \boldsymbol{u}_i^{+}$ can therefore also be decomposed as

$$\boldsymbol{u}_i = a_1(t_i)\boldsymbol{v}_1 + a_2(t_i)\boldsymbol{v}_2, \quad \boldsymbol{u}_i^{+} = a_1(t_i+\Delta t)\boldsymbol{v}_1 + a_2(t_i+\Delta t)\boldsymbol{v}_2 \tag{2.20}$$

for vectors $\boldsymbol{v}_1, \boldsymbol{v}_2 \in \mathbb{R}^p$ consisting of the values of ϕ_1, ϕ_2 at the points of the chosen spatial window,

$$\boldsymbol{v}_1 := [\,\phi_1(x_1) \quad \ldots \quad \phi_1(x_p)\,]^{\top}, \quad \boldsymbol{v}_2 := [\,\phi_2(x_1) \quad \ldots \quad \phi_2(x_p)\,]^{\top}. \tag{2.21}$$

The vectors $\boldsymbol{v}_1, \boldsymbol{v}_2$ therefore represent intrinsic mode shapes with which the observed snapshot data can be described, and their span $\mathscr{S} := \mathrm{sp}(\boldsymbol{v}_1, \boldsymbol{v}_2) \subset \mathbb{R}^p$ is an appropriate

https://doi.org/10.1017/jfm.2013.426 Published online by Cambridge University Press

low-dimensional subspace in which to identify the snapshot dynamics. This subspace can be represented as the image of the matrix

$$\boldsymbol{L} := \begin{bmatrix} \uparrow & \uparrow \\ \boldsymbol{v}_1/c & \boldsymbol{v}_2/c \\ \downarrow & \downarrow \end{bmatrix} \in \mathbb{R}^{p\times 2}, \tag{2.22}$$

where $c := \|\boldsymbol{v}_1\|_2 = \|\boldsymbol{v}_2\|_2$. Furthermore, since $\boldsymbol{v}_1, \boldsymbol{v}_2$ are orthogonal, the constraint $\boldsymbol{L}^\top \boldsymbol{L} = \boldsymbol{I}$ appearing in (2.11) is satisfied.

(ii) *Low-order dynamics* $\boldsymbol{M}$*:* by (2.20), the flow dynamics depend entirely on the weight functions $a_1(t), a_2(t)$ which satisfy

$$\frac{\mathrm{d}}{\mathrm{d}t}\begin{bmatrix} a_1(t) \\ a_2(t) \end{bmatrix} = \mathrm{e}^{\gamma t}\begin{bmatrix} -\gamma\sin(\omega t) - \omega\cos(\omega t) \\ \gamma\cos(\omega t) - \omega\sin(\omega t) \end{bmatrix} = \begin{pmatrix} \gamma & -\omega \\ \omega & \gamma \end{pmatrix}\begin{bmatrix} a_1(t) \\ a_2(t) \end{bmatrix}. \tag{2.23}$$

Since we want $\boldsymbol{M}$ to represent the evolution of the weights over Δt, we obtain

$$\begin{bmatrix} a_1(t_i + \Delta t) \\ a_2(t_i + \Delta t) \end{bmatrix} = \boldsymbol{M}\begin{bmatrix} a_1(t_i) \\ a_2(t_i) \end{bmatrix}, \quad \boldsymbol{M} := \mathrm{e}^{\begin{pmatrix} \gamma & -\omega \\ \omega & \gamma \end{pmatrix}\Delta t}. \tag{2.24}$$

Combining the above expression for $\boldsymbol{M}$ with (2.20) and (2.22), the relation between each snapshot pair $(\boldsymbol{u}_i, \boldsymbol{u}_i^+)$ can be written simply as

$$\boldsymbol{u}_i^+ = \begin{bmatrix} \boldsymbol{v}_1 & \boldsymbol{v}_2 \end{bmatrix}\begin{bmatrix} a_1(t_i + \Delta t) \\ a_2(t_i + \Delta t) \end{bmatrix} = \begin{bmatrix} \boldsymbol{v}_1 & \boldsymbol{v}_2 \end{bmatrix}\boldsymbol{M}\begin{bmatrix} a_1(t_i) \\ a_2(t_i) \end{bmatrix} = \boldsymbol{L}\boldsymbol{M}\boldsymbol{L}^\top \boldsymbol{u}_i \tag{2.25}$$

which is the form of the dynamics in (2.11). Finally, note that the rank constrained eigenvalues λ^{OMD} given by (2.15) are the eigenvalues $\gamma \pm \mathrm{i}\omega$ of

$$\begin{pmatrix} \lambda & -\omega \\ \omega & \lambda \end{pmatrix}. \tag{2.26}$$

Hence, the temporal growth rate γ and frequency ω of the flow (2.18) are exactly identified by solving the OMD optimization (2.11).

Since the underlying dynamics of the flow (2.18) are linear and noise-free, both the DMD and OMD methods will theoretically be able to exactly extract the eigenvalue information. In § 5, the performance of both techniques are analysed for this example when the snapshot data is corrupted with Gaussian noise. In the presence of noise, neither method is able to exactly identify the true system eigenvalues. However, the OMD method (2.11) is shown to consistently outperform DMD in this case.

2.4. *Relationship between DMD and OMD*

DMD (2.5) is a restricted case of the OMD (2.11). To see this, suppose that instead of optimizing (2.11) over both variables, we assume that $\boldsymbol{L}$ is fixed and that the optimization is performed over the *single variable* $\boldsymbol{M}$. In other words, a low-dimensional subspace of the flow field data is selected *a priori* and we search only for the best dynamical representation of the flow on that subspace. Since the best dynamics will depend on the particular subspace chosen, we denote the solution of this restricted optimization problem by $\boldsymbol{M}^*(\boldsymbol{L})$.

https://doi.org/10.1017/jfm.2013.426 Published online by Cambridge University Press

	DMD	OMD
Low-order subspace basis	$\boldsymbol{U}$	$\boldsymbol{L}$
Low-order dynamics	$\tilde{\boldsymbol{S}}$	$\boldsymbol{M}$
Eigenvalues	$\lambda_i^{DMD} = \frac{1}{\Delta t}\log\lambda_i(\tilde{\boldsymbol{S}})$	$\lambda_i^{OMD} = \frac{1}{\Delta t}\log\lambda_i(\boldsymbol{M})$
Dynamic modes	$\Phi_i^{DMD} = \boldsymbol{U}\boldsymbol{y}_i$	$\Phi_i^{OMD} = \boldsymbol{L}\boldsymbol{z}_i$

TABLE 1. Structural components of the DMD and OMD flow models. When $\boldsymbol{L} = \boldsymbol{U}$ the OMD method is equivalent to DMD.

It is in fact possible to find an analytical expression for $\boldsymbol{M}^*(\boldsymbol{L})$ by equating the partial derivative

$$\frac{\partial\left\|\boldsymbol{A} - \boldsymbol{L}\boldsymbol{M}\boldsymbol{L}^{\top}\boldsymbol{B}\right\|^2}{\partial \boldsymbol{M}} = 2\left[-\boldsymbol{L}^{\top}\boldsymbol{B}\boldsymbol{A}^{\top}\boldsymbol{L} + \boldsymbol{L}^{\top}\boldsymbol{B}\boldsymbol{B}^{\top}\boldsymbol{L}\boldsymbol{M}^{\top}\right] \tag{2.27}$$

to zero, which implies that

$$\boldsymbol{M}^*(\boldsymbol{L}) := \boldsymbol{L}^{\top}\boldsymbol{A}\boldsymbol{B}^{\top}\boldsymbol{L}\left(\boldsymbol{L}^{\top}\boldsymbol{B}\boldsymbol{B}^{\top}\boldsymbol{L}\right)^{-1}. \tag{2.28}$$

Now consider the particular case when $\boldsymbol{L}$ is fixed to be the first r columns of $\boldsymbol{U}$, where $\boldsymbol{B} = \boldsymbol{U}\boldsymbol{\Sigma}\boldsymbol{V}^{\top}$ is the compact singular value decomposition of $\boldsymbol{B}$. In other words, the low-dimensional subspace represented by $\boldsymbol{L}$ is fixed to be an r-dimensional POD basis. Under this restriction (2.28) becomes

$$\boldsymbol{M}^*(\boldsymbol{U}) = \boldsymbol{U}^{\top}\boldsymbol{A}\boldsymbol{B}^{\top}\boldsymbol{U}\left(\boldsymbol{U}^{\top}\boldsymbol{B}\boldsymbol{B}^{\top}\boldsymbol{U}\right)^{-1} = \boldsymbol{U}^{\top}\boldsymbol{A}\boldsymbol{V}\boldsymbol{\Sigma}^{-1} = \tilde{\boldsymbol{S}}. \tag{2.29}$$

Recalling that $\tilde{\boldsymbol{S}}$ is the matrix from (2.9) used in the DMD construction, it is now clear that if $\boldsymbol{L} = \boldsymbol{U}$, then $\lambda_i^{OMD} = \lambda_i^{DMD}$ and $\Phi_i^{OMD} = \Phi_i^{DMD}$.

Consequently, DMD can be calculated as a special case of the OMD optimization problem (2.11). Furthermore, this relation implies that DMD can be interpreted as producing low-order dynamics which are a projection of the flow onto a POD subspace, followed by a time step governed by $\tilde{\boldsymbol{S}}$. Viewed in this way as a rank-constrained optimization of the form (2.11), the structural components of DMD are summarized in table 1.

It is now apparent that the DMD method is restrictive in the sense that the projection is onto a fixed POD subspace. Since POD modes, especially in the case of randomly sampled data, do not intrinsically contain any dynamical information about the flow, it is not clear that $\boldsymbol{L} = \boldsymbol{U}$ is the optimal choice of low-dimensional subspace basis. Indeed, the restriction to a fixed basis in DMD can result in significant underperformance of DMD in some cases. We give such an example in appendix B. This motivates solving (2.11) in which both the subspace represented by $\boldsymbol{L}$ and the dynamics $\boldsymbol{M}$ are searched for simultaneously.

The difficulty in solving (2.11) is that the problem is non-convex. Our approach to the problem is to use techniques from matrix manifold theory (Absil, Mahony & Sepulchre 2008) which are employed in the § 4 to construct a method, Algorithm 1, to solve the OMD problem (2.11).

https://doi.org/10.1017/jfm.2013.426 Published online by Cambridge University Press

3. Koopman modes

Before proceeding to the numerical solution of the OMD problem (2.11), we explain the relation between OMD, DMD and a related identification method in (Chen *et al.* 2012) referred to as 'optimized DMD' or opt-DMD in the context of the Koopman modes and eigenvalues of the underlying fluid system.

3.1. *A Koopman mode interpretation of OMD*

An introduction to Koopman modes, and their relation to DMD, is given by Rowley *et al.* (2009) and Mezić (2013) and we therefore present only a brief summary here.

Suppose that the underlying velocity field is represented by an element z of a manifold Z and evolves over a time step Δt to a new state $z^+ \in Z$ via the dynamical system $z^+ = F(z)$. The Koopman (or composition) operator C is defined to act on the space of one-dimensional observables $\gamma : Z \to \mathbb{C}$ via the composition formula

$$C\gamma := \gamma \circ F. \tag{3.1}$$

An *observable* is simply a scalar-valued function on the space Z. Since DMD and OMD modes are in general complex, it is convenient to work with complex-valued observables even if the underlying data are real. Now, $C\gamma : Z \to \mathbb{C}$ is itself an observable on Z with $(C\gamma)(z) = \gamma(F(z)) = \gamma(z^+)$. Since C is a linear operator, we may assume that it has an infinite basis of linearly independent eigenfunctions $\phi_i^C : Z \to \mathbb{C}$ and associated eigenvalues λ_i^C.

To consider data arising from experiments or simulations in fluid mechanics, it is convenient to work with a vector-valued observable $g : Z \to \mathbb{C}^p$ where, for example, each component of $g(z)$ represents the velocity at a particular point in the instantaneous flow field z. A standard assumption is that there exist vectors $\boldsymbol{v}_j^K \in \mathbb{C}^p$ such that

$$g(z) = \sum_{j=1}^{\infty} \boldsymbol{v}_j^K \phi_j^C(z). \tag{3.2}$$

That is, it is assumed that each of the components of g lies in the span of the Koopman eigenfunctions ϕ_j^C. Following (Budišić, Mohr & Mezić 2012), define the space of all such observables by $\mathscr{F}^p$. The vectors v_j^K are referred to as the *Koopman modes* of the mapping F corresponding to the observable g. Since each ϕ_j^C is an eigenfunction of C,

$$g(z^+) = \sum_{j=1}^{\infty} \boldsymbol{v}_j^K (C\phi_j^C)(z) = \sum_{j=1}^{\infty} \boldsymbol{v}_j^K \lambda_j^C \phi_j^C(z). \tag{3.3}$$

The compelling aspect of this analysis is that the above equality is exact and that the (nonlinear) evolution $g(z) \mapsto g(z^+)$ of the observable can be described in terms of the eigenvalues and eigenfunctions of the (linear) Koopman operator. Furthermore, (3.3) allows a natural extension of the Koopman operator to act on such a vector-valued observable $g = (g_1, \ldots, g_p)^\top \in \mathscr{F}^p$ via

$$(Cg)(z) := \sum_{j=1}^{\infty} \boldsymbol{v}_j^K (C\phi_j^C)(z) = \begin{pmatrix} (Cg_1)(z) \\ \vdots \\ (Cg_p)(z) \end{pmatrix} = g(z^+), \quad z \in Z. \tag{3.4}$$

https://doi.org/10.1017/jfm.2013.426 Published online by Cambridge University Press

Now, suppose that the data ensemble arises in terms of an observable g such that $(\boldsymbol{u}_j, \boldsymbol{u}_j^+) = (g(z_j), g(z_j^+))$. Then, using (3.4), the OMD optimization problem (2.11) can be written in component form as

$$\min_{\boldsymbol{L},\boldsymbol{M}} \sum_{j=1}^{N} \left\| (Cg)(z_j) - (\boldsymbol{L}\boldsymbol{M}\boldsymbol{L}^{\top} g)(z_j) \right\|_2^2, \tag{3.5}$$

where the observable $\boldsymbol{L}\boldsymbol{M}\boldsymbol{L}^{\top} g : Z \to \mathbb{C}^p$ is defined by $(\boldsymbol{L}\boldsymbol{M}\boldsymbol{L}^{\top} g)(z) := \boldsymbol{L}\boldsymbol{M}\boldsymbol{L}^{\top} g(z)$. Therefore, given the data ensemble arising from an observable $g \in \mathscr{F}^p$, OMD can be though of as providing the optimal (in a least-squares sense) approximation to the Koopman operator by a finite-rank operator of the form $\boldsymbol{L}\boldsymbol{M}\boldsymbol{L}^{\top} : \mathscr{F}^p \to \mathscr{F}^p$.

We now explain the nature of the approximation that the OMD modes Φ_i^{OMD} and eigenvalues λ_i^{OMD} provide to the Koopman modes $\boldsymbol{v}_j^K$ and eigenvalues λ_j^C. For the remainder of this section it will be assumed that the data ensemble is sequential in the sense that $\boldsymbol{u}_i^+ = \boldsymbol{u}_{i+1}$, i.e.

$$\boldsymbol{B} = (\boldsymbol{u}_1 \mid \cdots \mid \boldsymbol{u}_N) = \left(g(z_1) \mid \cdots \mid (C^{N-1} g)(z_1)\right) \tag{3.6a}$$

$$\boldsymbol{A} = (\boldsymbol{u}_2 \mid \cdots \mid \boldsymbol{u}_{N+1}) = \left((Cg)(z_1) \mid \cdots \mid (C^{N} g)(z_1)\right) \tag{3.6b}$$

where $z_1 \in Z$ is the initial point of the underlying flow from which the data was sampled.

Now, consider decision variables $\boldsymbol{L} \in \mathbb{R}^{p\times r}$ and $\boldsymbol{M} \in \mathbb{R}^{r\times r}$ appearing in the OMD problem (2.11). Assume that $\boldsymbol{M}$ is diagonalizable as $\boldsymbol{M} = \boldsymbol{T}\Lambda\boldsymbol{T}^{-1}$, define

$$\mathscr{V} := \boldsymbol{B}^{\top}\boldsymbol{L}(\boldsymbol{L}^{\top}\boldsymbol{B}\boldsymbol{B}^{\top}\boldsymbol{L})^{-1} \in \mathbb{R}^{N\times r} \tag{3.7}$$

and recall that, by (2.16), the OMD modes Φ_i^{OMD} are the columns of $\boldsymbol{L}\boldsymbol{T}$. Note also that the matrix $\mathscr{V}$ appears in (2.28) as a result of optimizing the OMD residual over $\boldsymbol{M}$ for a fixed choice of basis $\boldsymbol{L}$. A consequence is that an optimal solution pair $\boldsymbol{L}, \boldsymbol{M}$ necessarily satisfies

$$\boldsymbol{M} = \boldsymbol{L}^{\top}\boldsymbol{A}\mathscr{V}. \tag{3.8}$$

This choice of $\boldsymbol{M}$ is intrinsically linked to the approximation that OMD modes and eigenvalues provide to the system's Koopman modes and eigenvalues. To see why, consider the observables $\Phi_i^L : Z \to \mathbb{C}^p$ defined by

$$\Phi_i^L(z) := \sum_{j=1}^{N} v_{ji}\boldsymbol{L}\boldsymbol{L}^{\top} g(F^{j-1}(z)), \tag{3.9}$$

where $(v_{ij})_{i=1,j=1}^{N\times r} = \mathscr{V}\boldsymbol{T}$ and F is the mapping describing the evolution of the underlying fluid system over one time step Δt. Using (3.6) it can be seen that $\Phi_i^L(z_1) \in \mathbb{C}^p$ is the ith column of the matrix $\boldsymbol{L}\boldsymbol{L}^{\top}\boldsymbol{B}\mathscr{V}\boldsymbol{T}$. Furthermore, since $\boldsymbol{L}\boldsymbol{L}^{\top}\boldsymbol{B}\mathscr{V}\boldsymbol{T} = \boldsymbol{L}\boldsymbol{T}$ it follows from (2.16) that $\Phi_i^L(z_1) = \Phi_i^{OMD}$. In other words, the OMD modes are equal to the values of the observables Φ_i^L at the initial point $z_1 \in Z$ of the underlying flow from which the data was sampled.

Now, the value of each observable $(C\Phi_i^L)(\cdot)$ at the point z_1 can be calculated using the relation

$$\left(\left(C\Phi_1^L\right)(z_1) \mid \cdots \mid \left(C\Phi_r^L\right)(z_1)\right) = (\boldsymbol{L}\boldsymbol{T})\Lambda + \boldsymbol{L}(\boldsymbol{L}^{\top}\boldsymbol{A}\mathscr{V} - \boldsymbol{M})\boldsymbol{T} \tag{3.10}$$

https://doi.org/10.1017/jfm.2013.426 Published online by Cambridge University Press

which is proved in theorem 2 of appendix A. Therefore, if $\boldsymbol{L}, \boldsymbol{M}$ are optimal decision variables for OMD, then (3.8) implies that

$$(C\Phi_i^L)(z_1) = \lambda_i^{OMD}\Phi_i^L(z_1) = \lambda_i^{OMD}\Phi_i^{OMD}. \tag{3.11}$$

Hence, the observables $\Phi_i^L(\cdot)$ behave like vector-valued eigenfunctions of the Koopman operator with eigenvalues λ_i^{OMD} *at the point* z_1 and, furthermore, are equal to the OMD modes at that point: $\Phi_i^L(z_1) = \Phi_i^{OMD}$. In this sense, the OMD eigenvalues approximate a subset of the eigenvalues of the Koopman operator since, as is shown in lemma 1, the eigenvalues of $C : \mathscr{F}^p \to \mathscr{F}^p$ are the eigenvalues λ_j^C of the Koopman operator acting on scalar-valued observables.

We now link the OMD modes Φ_i^{OMD} with the Koopman modes v_i^K. Since $C : \mathscr{F}^p \to \mathscr{F}^p$ is linear, we assume it has a basis of vector-valued eigenfunctions $\Phi_i^C \in \mathscr{F}^p$. By assumption $g \in \mathscr{F}^p$ and, therefore, there exist scalars $\alpha_i \in \mathbb{C}$ such that

$$g(z) = \sum_{i=1}^{\infty} \alpha_i \Phi_i^C(z). \tag{3.12}$$

The interpretation of (3.11) is now that $(\lambda_i^{OMD}, \Phi_i^L)$ approximates the behaviour of a true eigenvalue–eigenfunction pair (λ_j^C, Φ_j^C) at the point $z_1 \in Z$. Assuming that the eigenvalue λ_j^C is simple with respect to the Koopman operator acting on scalar-valued observables, lemma 1 of appendix A implies that $\Phi_j^C = \boldsymbol{w}_j\phi_j^C$ for some $\boldsymbol{w}_j \in \mathbb{C}^p$. Using this relation to expand (3.12) in terms of the scalar-valued eigenfunctions ϕ_j^C, comparing the expression to (3.2) and invoking linear independence implies that $\boldsymbol{w}_j\alpha_j = \boldsymbol{v}_j^K$. Hence,

$$\Phi_i^{OMD} = \Phi_i^L(z_1) \approx \Phi_j^C(z_1) = \boldsymbol{v}_j^K\left(\alpha_j^{-1}\phi_j^C(z_1)\right). \tag{3.13}$$

In this sense each OMD mode Φ_i^{OMD} approximates a Koopman mode $\boldsymbol{v}_j^K$, up to a multiplicative scalar.

Interestingly, it is clear from (3.10) that equality holds in (3.11) for any decision variables $\boldsymbol{L}, \boldsymbol{M}$ satisfying (3.8). In other words, fixing $\boldsymbol{L}$ in (3.5) then optimizing over $\boldsymbol{M}$ only can be interpreted as providing an approximation to the Koopman eigenvalues and modes *for any* $\boldsymbol{L}$. The particular case when $\boldsymbol{L}$ is fixed equal to $\boldsymbol{U}$ therefore provides a Koopman mode interpretation of DMD. On the other hand OMD searches over all pairs $\boldsymbol{L}, \boldsymbol{M}$ for which equality holds in (3.11) to obtain the variables which provide the 'optimal' (in the least-squares sense of (3.5)) approximation to the Koopman operator of the finite-rank form $\boldsymbol{LML}^\top : \mathscr{F}^p \to \mathscr{F}^p$. It should be noted that the motivation for DMD in the literature is a slight modification of this argument. For the DMD case when $\boldsymbol{L}$ is fixed to be $\boldsymbol{U}$, because $\boldsymbol{UU}^\top g(z_i) = g(z_i)$ one may instead define the observables Φ_i^U without the projection term $\boldsymbol{UU}^\top$. The right-hand-side of (3.10) corresponding to this choice of observables is then $\boldsymbol{UT}\Lambda + (\boldsymbol{A} - \boldsymbol{UMU}^\top\boldsymbol{B})\boldsymbol{\mathscr{V}}\boldsymbol{T}$. Since DMD selects $\boldsymbol{M} = \tilde{\boldsymbol{S}}$ to minimize $\boldsymbol{A} - \boldsymbol{UMU}^\top\boldsymbol{B}$, a similar argument to the above implies that DMD approximates the Koopman eigenvalues and modes, albeit without equality in (3.11). Note that the resulting residual $\boldsymbol{A} - \boldsymbol{U}\tilde{\boldsymbol{S}}\boldsymbol{U}^\top\boldsymbol{B}$ is equal to the '$\boldsymbol{re}^\top$' term in Rowley *et al.* (2009, equation (3.12)) while $(\boldsymbol{A} - \boldsymbol{U}\tilde{\boldsymbol{S}}\boldsymbol{U}^\top\boldsymbol{B})\boldsymbol{\mathscr{V}}\boldsymbol{T}$ is equal to the '$\boldsymbol{\eta}_r\boldsymbol{e}^\top\boldsymbol{V}^{-1}$' term in Budišić *et al.* (2012, equation (57)).

Finally, it is important to emphasize that (3.11) does not imply that Φ_i^L is an eigenfunction of C, merely that Φ_i^L behaves like an eigenfunction at the single point $z_1 \in Z$. Furthermore, (3.11) does not quantify the quality of the approximation that

https://doi.org/10.1017/jfm.2013.426 Published online by Cambridge University Press

the observables Φ_i^L provide to the true Koopman eigenfunctions Φ_i^C. Essentially, this is due to the fact that we only have information concerning a single point $z_1 \in Z$ of the underlying fluid system. For this reason, we emphasize that it is not currently possible to say whether either DMD or OMD provides a better approximation to the true Koopman modes $\boldsymbol{v}_j^K$ and eigenvalues λ_j^C.

3.2. *Opt-DMD*

Koopman modes also provide the motivation for the recently proposed opt-DMD algorithm of Chen *et al.* (2012). To calculate opt-DMD, the following optimization problem is solved:

$$\begin{aligned} \min_{\boldsymbol{V},\boldsymbol{T}} \quad & \|\boldsymbol{B} - \boldsymbol{V}\boldsymbol{T}\|^2 \\ \text{s.t.} \quad & \boldsymbol{V} \in \mathbb{R}^{p\times r} \\ & \boldsymbol{T} = \begin{pmatrix} 1 & \lambda_1 & \lambda_1^2 & \dots & \lambda_1^{N-1} \\ 1 & \lambda_2 & \lambda_2^2 & \dots & \lambda_2^{N-1} \\ \vdots & \vdots & \vdots & & \vdots \\ 1 & \lambda_r & \lambda_r^2 & \dots & \lambda_r^{N-1} \end{pmatrix} \quad \text{some } \lambda_i \in \mathbb{R}. \end{aligned} \tag{3.14}$$

The resulting mode shapes $\Phi_i^{opt\text{-}DMD}$ are the columns of the optimal variable $\boldsymbol{V}$ with eigenvalues $\lambda_i^{opt\text{-}DMD}$ given by the corresponding entries of the optimal matrix $\boldsymbol{T}$. The link between opt-DMD and OMD is given by the fact, proven in theorem 3 of appendix A, that (3.14) is equivalent to

$$\begin{aligned} \min_{\boldsymbol{L},\boldsymbol{M},\xi_1} \quad & \sum_{i=1}^{N} \|\boldsymbol{u}_i - (\boldsymbol{L}\boldsymbol{M}\boldsymbol{L}^\top)^{i-1}\xi_1\|_2^2 \\ \text{s.t.} \quad & \boldsymbol{L}^\top\boldsymbol{L} = \boldsymbol{I}, \ \ \boldsymbol{M} \text{ diagonalizable}, \ \ \xi_1 \in \mathrm{Im}(\boldsymbol{L}). \end{aligned} \tag{3.15}$$

Thus, opt-DMD can be thought of as searching for the best (in a least-squares sense) linear trajectory $\{\xi_1, \boldsymbol{X}\xi_1, \dots, \boldsymbol{X}^{N-1}\xi_1\}$ to fit the data $\{\boldsymbol{u}_1, \dots, \boldsymbol{u}_N\}$, under the restrictions: (i) the linear process has the low-order form $\boldsymbol{X} = \boldsymbol{L}\boldsymbol{M}\boldsymbol{L}^\top$; and (ii) the initial value ξ_1 of the trajectory lies in the subspace spanned by $\boldsymbol{L}$.

Note that while the DMD and OMD methods do not actually require a sequential data ensemble to work, opt-DMD does require sequential data. The reader will also observe that the objective function in (3.14) is an Nth-order polynomial function of the parameters λ_i, where N is the number of data samples. As noted by Chen *et al.* (2012), the resulting optimization problem is very difficult to solve, and the authors proposed a randomized solution approach based on simulated annealing. In contrast, we show in § 4 that a solution to the OMD optimization problem (2.11) can be computed using a standard gradient-based algorithm which require only standard linear algebraic operations, is deterministic and is guaranteed to converge.

The original Koopman-mode motivation for opt-DMD is explained by the fact that the Vandermonde structure of $\boldsymbol{T}$ in (3.14) implies that the data sequence can be represented as

$$\boldsymbol{u}_i = \sum_{j=1}^{r} (\lambda_j^{opt\text{-}DMD})^{i-1} \Phi_j^{opt\text{-}DMD} + \boldsymbol{r}_i \tag{3.16}$$

where $\boldsymbol{r}_i$ are components of the associated optimization residual. On the other hand, a recursive application of (3.3) implies that each $\boldsymbol{u}_i$ can alternatively be written in terms

https://doi.org/10.1017/jfm.2013.426 Published online by Cambridge University Press

of the true Koopman modes and eigenvalues as

$$\boldsymbol{u}_i = \sum_{j=1}^{\infty} \boldsymbol{v}_j^K (\lambda_j^C)^{i-1} \phi_j^C(z_1). \tag{3.17}$$

Since (3.16) resembles a finite truncation of (3.17), it is argued by Chen *et al.* (2012) that the opt-DMD modes and eigenvalues approximate a subset of the Koopman modes and eigenvalues. Again, there is an unquantified approximation involved in this argument, since even small residuals $\boldsymbol{r}_i$ do not guarantee that the identified modes and eigenvalues are close to a subset of the true Koopman modes and eigenvalues.

3.3. *Optimal Koopman mode identification?*

We end this section by briefly reiterating that, at the current state of the literature, it is not clear which of DMD, OMD or opt-DMD produces the best approximation to the Koopman modes and eigenvalues. This is since the arguments used to relate the Koopman modes to the modes produced by each algorithm all require an approximation step, as described in §§ 3.1 and 3.2, and the quality of the approximation cannot be formally quantified for any of the methods.

However, since OMD (and DMD when $\boldsymbol{L}$ is fixed to be $\boldsymbol{U}$) seeks to minimize the least-squares sum of the residuals

$$(Cg)(z_j) - (\boldsymbol{L}\boldsymbol{M}\boldsymbol{L}^\top g)(z_j), \tag{3.18}$$

it can be thought of as providing a finite rank approximation $\boldsymbol{L}\boldsymbol{M}\boldsymbol{L}^\top : \mathscr{F}^p \to \mathscr{F}^p$ to the Koopman operator. On the other hand, opt-DMD seeks to minimize the least-squares sum of residuals

$$(C^{j-1}g)(z_1) - (\boldsymbol{L}\boldsymbol{M}\boldsymbol{L}^\top)^{j-1}\xi_1 \tag{3.19}$$

for some $\xi_1 \in \mathrm{Im}(\boldsymbol{L})$. In this case, the direct link between C and $\boldsymbol{L}\boldsymbol{M}\boldsymbol{L}^\top$ is less obvious and, instead, the similarity of the sums (3.16) and (3.17) motivates the link between opt-DMD and the Koopman operator. To the best of the authors' knowledge it is therefore an important open problem to formally quantify the approximation that each of the three methods provides to the true Koopman modes and eigenvalues. This will form the basis of future research.

4. Solution to the OMD minimization problem

The aim is to construct optimal variables $\boldsymbol{L}$ and $\boldsymbol{M}$ which minimize the norm in (2.11). For a fixed $\boldsymbol{L}$, the minimum $\boldsymbol{M}^*(\boldsymbol{L})$ over the variable $\boldsymbol{M}$ is given by (2.28). Hence, (2.11) can be solved by substituting the expression for $\boldsymbol{M}^*(\boldsymbol{L})$ into the norm in (2.11) and optimizing over the single variable $\boldsymbol{L}$. Performing this substitution gives

$$\left\|\boldsymbol{A} - \boldsymbol{L}\boldsymbol{M}^*(\boldsymbol{L})\boldsymbol{L}^\top\boldsymbol{B}\right\|^2 = \left\|\boldsymbol{A} - \boldsymbol{L}\boldsymbol{L}^\top\boldsymbol{A}\boldsymbol{Q}(\boldsymbol{L})\right\|^2 = \|\boldsymbol{A}\|^2 - \left\|\boldsymbol{L}^\top\boldsymbol{A}\boldsymbol{Q}(\boldsymbol{L})\right\|^2, \tag{4.1}$$

where $\boldsymbol{Q}(\boldsymbol{L}) := \boldsymbol{B}^\top\boldsymbol{L}\left(\boldsymbol{L}^\top\boldsymbol{B}\boldsymbol{B}^\top\boldsymbol{L}\right)^{-1}\boldsymbol{L}^\top\boldsymbol{B}$ is an orthogonal projection defined in terms of $\boldsymbol{L}$. Consequently, the two-variable minimization problem (2.11) is equivalent to the single-variable maximization problem

$$\begin{aligned} \max \quad & g(\boldsymbol{L}) := \left\|\boldsymbol{L}^\top\boldsymbol{A}\boldsymbol{Q}(\boldsymbol{L})\right\|^2 \\ \text{s.t.} \quad & \boldsymbol{L} \in \mathbb{R}^{p\times r}, \quad \boldsymbol{L}^\top\boldsymbol{L} = \boldsymbol{I}, \\ & \boldsymbol{Q}(\boldsymbol{L}) = \boldsymbol{B}^\top\boldsymbol{L}\left(\boldsymbol{L}^\top\boldsymbol{B}\boldsymbol{B}^\top\boldsymbol{L}\right)^{-1}\boldsymbol{L}^\top\boldsymbol{B}. \end{aligned} \tag{4.2}$$

https://doi.org/10.1017/jfm.2013.426 Published online by Cambridge University Press

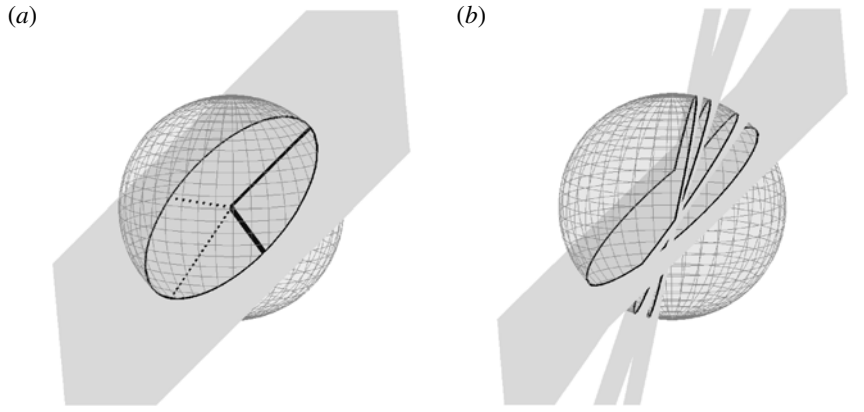


FIGURE 2. The Grassman manifold $G_{2,3}$. (*a*) Variables for (4.2) are matrices whose columns are orthogonal elements of the unit sphere. In the case depicted, variables $\boldsymbol{L}_1, \boldsymbol{L}_2 \in \mathbb{R}^{3\times 2}$ have columns as solid and dotted unit vectors, respectively. Both matrices represent the same subspace and hence the same element of $G_{2,3}$. Furthermore, $g(\boldsymbol{L}_1) = g(\boldsymbol{L}_2)$. (*b*) A sequence of elements of $G_{2,3}$, representing 'subspace variables' of (4.2).

If a maximizer $\boldsymbol{L}^*$ to (4.2) can be found, it provides a solution pair $(\boldsymbol{L}^*, \boldsymbol{M}^*(\boldsymbol{L}^*))$ to (2.11), with $\boldsymbol{M}^*(\boldsymbol{L}^*)$ given by (2.28). Algorithm 1, stated below, provides an iterative method for solving (4.2). It is a conjugate-gradient-based algorithm, tailored to exploit intrinsic properties of (4.2) by using tools from matrix manifold theory.

The fundamental property of (4.2) which must be utilized by any gradient-based algorithm is that it is an optimization over *r-dimensional subspaces* of $\mathbb{R}^p$, rather than simply a matrix-valued optimization. To see why this is true, note first that due to the constraint $\boldsymbol{L}^\top \boldsymbol{L} = \boldsymbol{I}$, each feasible variable $\boldsymbol{L} \in \mathbb{R}^{p\times r}$ represents an orthonormal basis for the subspace $\mathrm{Im}(\boldsymbol{L}) \subset \mathbb{R}^p$. Hence, if $\boldsymbol{L}_1, \boldsymbol{L}_2$ are two variables representing the same subspace then there exists an orthogonal transformation $\boldsymbol{P} \in \mathbb{R}^{r\times r}$ such that $\boldsymbol{L}_1 = \boldsymbol{L}_2\boldsymbol{P}$. Consequently,

$$g(\boldsymbol{L}_1) = f(\boldsymbol{L}_2\boldsymbol{P}) = \|\boldsymbol{P}^\top \boldsymbol{L}_2^\top \boldsymbol{A}\boldsymbol{Q}(\boldsymbol{L}_2\boldsymbol{P})\| = \|\boldsymbol{L}_2^\top \boldsymbol{A}\boldsymbol{Q}(\boldsymbol{L}_2)\| = g(\boldsymbol{L}_2), \tag{4.3}$$

which implies that it is only the subspace represented by the variable $\boldsymbol{L}$ which determines the value g. The search for an optimal value of g must therefore be performed over the manifold of r-dimensional subspaces of $\mathbb{R}^p$, known as the *Grassman manifold* $G_{r,p}$.

Each element of the Grassman manifold $G_{r,p}$, i.e. each r-dimensional subspace $\mathscr{S} \subset \mathbb{R}^p$, is represented by *any* matrix with orthogonal columns which span that subspace $\mathscr{S}$. For example, elements of the manifold $G_{2,3}$ depicted in figure 2 are planes in $\mathbb{R}^3$. Each plane can be represented by any matrix $\boldsymbol{L} \in \mathbb{R}^{2\times 3}$ whose columns are a pair of orthogonal unit vectors in that plane, as shown in figure 2(*a*). An effective search algorithm over a Grassman manifold must take into account this fact that each point in the manifold is represented by infinitely many matrices. In particular, search directions will be chosen along geodesics of the manifold, which represent the shortest distance between two given subspaces, while the search direction itself is determined by the gradient ∇g at the current point on the manifold.

In (Edelman, Arias & Smith 1998), the following formulae are given for the gradient and geodesic curves on a Grassman manifold. Given an element of $G_{r,p}$

https://doi.org/10.1017/jfm.2013.426 Published online by Cambridge University Press

represented by a matrix $\boldsymbol{L}_0 \in \mathbb{R}^{r\times p}$, the gradient of a function g at $\boldsymbol{L}_0$ is given by

$$\nabla g = (\boldsymbol{I} - \boldsymbol{L}_0\boldsymbol{L}_0^\top)g_{\boldsymbol{L}_0}, \tag{4.4}$$

where $g_{\boldsymbol{L}_0} := (\partial g/\partial \boldsymbol{L})(\boldsymbol{L}_0)$. The geodesic passing through $\boldsymbol{L}_0$ in the direction ∇g is given by the parameterized formula

$$\boldsymbol{L}_0(t) = \boldsymbol{L}_0\boldsymbol{V}\cos(\Sigma t)\boldsymbol{V}^\top + \boldsymbol{U}\sin(\Sigma t)\boldsymbol{V}^\top, \quad t \in [0, 1], \tag{4.5}$$

where $\nabla g = \boldsymbol{U}\Sigma\boldsymbol{V}^\top$ is the compact singular value decomposition of ∇f. These expressions are used in Algorithm 1 to provide a solution to (4.2).

Algorithm 1 Conjugate gradient algorithm for solution of (4.1)

1: set initial $\boldsymbol{L}_0 \in \mathbb{R}^{p\times r}$ satisfying $\boldsymbol{L}_0^\top\boldsymbol{L}_0 = \boldsymbol{I}$.
2: compute initial gradient $\boldsymbol{G}_0 := (\boldsymbol{I} - \boldsymbol{L}_0\boldsymbol{L}_0^\top)g_{\boldsymbol{L}_0}$ and search direction $\boldsymbol{H}_0 := -\boldsymbol{G}_0$
3: **repeat** {for $k = 0, 1, 2, \ldots$}
4: compute minimizer $t_{min} \in [0, 1]$ of $g(\boldsymbol{L}_k(t))$ over the geodesic curve

$$\boldsymbol{L}_k(t) := \boldsymbol{L}_k\boldsymbol{V}\cos(\Sigma t)\boldsymbol{V}^\top + \boldsymbol{U}\sin(\Sigma t)\boldsymbol{V}^\top, \quad t \in [0, 1],$$

in direction $\boldsymbol{H}_k = \boldsymbol{U}\Sigma\boldsymbol{V}^\top$
5: update subspace basis $\boldsymbol{L}_{k+1} := \boldsymbol{L}_k(t_{min})$
6: update gradient

$$\boldsymbol{G}_{k+1} := (\boldsymbol{I} - \boldsymbol{L}_{k+1}\boldsymbol{L}_{k+1}^\top)g_{\boldsymbol{L}_{k+1}}$$

7: update (conjugate-gradient) search direction

$$\boldsymbol{H}_{k+1} := G_{k+1} + \Delta_{k+1}$$

8: **until** $g(\boldsymbol{L}_{k+1}) - g(\boldsymbol{L}_k) <$ tolerance
9: **return** Optimal low-order subspace basis $\boldsymbol{L}_{k+1}$ and dynamics $\boldsymbol{M}(\boldsymbol{L}_{k+1})$.

Algorithm 1 is described in Edelman *et al.* (1998) and is included here for completeness. With respect to the particular problem (4.2), specific expressions for the partial derivative $g_{\boldsymbol{L}_0} := (\partial g/\partial \boldsymbol{L})(\boldsymbol{L}_0)$ and the conjugate-gradient correction Δ_{k+1} are given in appendix C. It should be noted that other algorithmic techniques, such as Newton's method, have been developed for subspace-valued optimization and may therefore also be applied to (4.2). The reader is referred to (Edelman *et al.* 1998; Goulart, Wynn & Pearson 2012) for more details. A MATLAB implementation of Algorithm 1 and its application to the example of § 5 is available at http://control.ee.ethz.ch/~goularpa/omd/.

4.1. *Computational performance*

We now compare the computational performance of OMD with respect to DMD. Each algorithm is applied to a data ensembles taken from an experimental data set of velocity measurements for flow over a backward facing step. The experiment is described in detail in § 6. Each snapshot contains velocity data at $p = 15\,600$ pixels and data ensembles were selected to contain $N = 100$, 200, 500 and 1000 snapshots. For each data ensemble, reduced-order models of order $r = 10$, 20, 50 and 100 were computed using both the DMD and OMD methods. The OMD Algorithm 1 was applied to each data ensemble with tolerance 10^{-5} in each case. Table 2

https://doi.org/10.1017/jfm.2013.426 Published online by Cambridge University Press

	$r = 10$		$r = 20$		$r = 50$		$r = 100$	
$N = 100$	0.94	(0.20)	4.15	(0.20)	24.65	(0.20)	7.83	(0.20)
$N = 200$	2.56	(0.50)	8.04	(0.50)	11.45	(0.50)	28.00	(0.50)
$N = 500$	4.17	(1.82)	11.40	(1.82)	39.90	(1.82)	113.65	(1.82)
$N = 1000$	9.15	(6.20)	16.72	(6.20)	69.49	(6.20)	157.00	(6.20)

TABLE 2. Computational times (s) for the OMD and DMD algorithms (DMD times in parentheses) implemented on a data ensemble containing N snapshots and producing a model of order r. Each snapshot has $p = 15\,600$ data points.

compares the computation times for the OMD and DMD algorithms (DMD times in parentheses). Since the OMD algorithm is iterative it requires more computation time than DMD. However, even for a relatively large number of snapshots, neither method represents a particularly burdensome computation; for example, with data parameters $p = 15\,600$, $N = 1000$, $r = 100$ the OMD algorithm was solved to tolerance in less than 3 min. All computations were performed using MATLAB on a standard desktop PC with a 2.2 GHz quad-core Intel i7 processor and 8 GB RAM running Mac OS X 10.6.

Note that even if the desired size r of the reduced model is small, it may still be the case that N is large, i.e. we may wish to use a large ensemble of snapshot data. In this situation, each evaluation of the function g required in step 4 of Algorithm 1 may be costly since it requires evaluation of the products $\boldsymbol{L}^{\top}\boldsymbol{B}, \boldsymbol{L}^{\top}\boldsymbol{A} \in \mathbb{R}^{r\times N}$. If it is the case that this presents a computational issue, a method of reducing the dimension of the optimization problem is presented in appendix D.

5. Comparison with DMD using a synthetic data ensemble

To compare the performance of the OMD with DMD, we analyse the ability of each technique to extract eigenvalue information from data ensembles sampled from the simple sinusoidal flow

$$f(x, t) := \sin(kx - \omega t)\mathrm{e}^{\gamma t}, \tag{5.1}$$

corrupted with additive Gaussian noise.

This flow was used by Duke, Soria & Honnery (2012) to analyse the DMD algorithm. Algorithm performance is determined by the *relative growth rate error* statistic. Specifically, let γ_{DMD} and γ_{OMD} denote the respective growth rates associated with the most unstable eigenvalues calculated by DMD and Algorithm 1:

$$\gamma_{DMD} := \max\left\{\mathrm{Re}(\lambda_1^{DMD}), \mathrm{Re}(\lambda_2^{DMD})\right\}, \quad \gamma_{OMD} := \max\left\{\mathrm{Re}(\lambda_1^{OMD}), \mathrm{Re}(\lambda_2^{OMD})\right\} \tag{5.2}$$

Then the relative growth rate errors associated with each algorithm are defined by

$$\epsilon_{DMD} := \left|\frac{\gamma_{DMD} - \gamma}{\gamma}\right|, \quad \epsilon_{OMD} := \left|\frac{\gamma_{OMD} - \gamma}{\gamma}\right|. \tag{5.3}$$

Thus ϵ_{DMD} and ϵ_{OMD} measure the quality of approximation that the extracted low-order dynamics provide to the true temporal growth rate γ.

Relative growth rate errors were calculated using data simulated from (5.1). Growth rate and spatial frequency were chosen to be $\gamma = k = 1$, while temporal frequency was varied over the range $\omega \in [0.6, 1.6]$. The number of temporal snapshots was $N = 50$, taken at time intervals $\mathrm{d}t = \pi/100$, while $p = 200$ spatial samples were

https://doi.org/10.1017/jfm.2013.426 Published online by Cambridge University Press

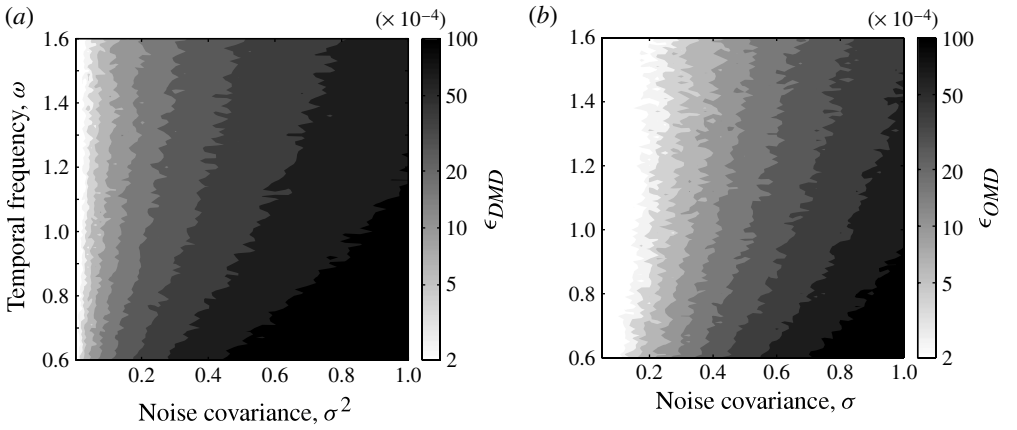


FIGURE 3. Relative growth rate errors for (*a*) ϵ_{DMD} and (*b*) ϵ_{OMD} associated with DMD and Algorithm 1, respectively. Errors calculated as the average of 10^3 simulations for varying temporal frequencies $\omega \in [0.6, 1.6]$ and additive Gaussian noise with covariances $\sigma^2 \in [0.05^2, 1]$. White areas denote growth rate error below tolerance $\epsilon = 10^{-4}$.

taken at intervals $\mathrm{d}x = \pi/100$. After arranging snapshots into 'before' and 'after' matrices $\boldsymbol{A}, \boldsymbol{B} \in \mathbb{R}^{p\times N}$, the data was corrupted by adding zero-mean Gaussian noise with covariance $\sigma^2 \in [0.05^2, 1]$. At each covariance and temporal frequency pair $(\sigma^2, \omega) \in [0.05^2, 1] \times [0.6, 1.6]$, 10^3 data ensembles were created and both DMD and Algorithm 1 were applied to each simulation ensemble. Calculation of the DMD eigenvalues was performed using the method described by Duke *et al.* (2012) with a rank-reduction ratio of 10^{-1}. A rank reduction ratio of 10^{-1} refers to the truncation of the matrix Σ of singular values used in the calculation of DMD (see § 2.1) to contain only those values within 10 % of the most energetic singular value.

Figure 3(*a*) depicts the growth rate errors ϵ_{DMD} and figure 3(*b*) the errors ϵ_{OMD}. For both algorithms, performance improves as temporal frequency increases, since more wavelengths are contained in the data ensemble. Performance also improves as noise covariance decreases. However, it is apparent that for all temporal frequencies in the simulation range, the error ϵ_{OMD} associated with Algorithm 1 is lower than the error ϵ_{DMD} associated with DMD. Hence, Algorithm 1 provides an improvement over DMD for the considered data parameters.

To analyse this performance advantage further, the percentage improvement

$$p_\epsilon := 100\,\% \cdot (\epsilon_{DMD} - \epsilon_{OMD})/\epsilon_{DMD} \tag{5.4}$$

is plotted in figure 4(*a*). The horizontal banded structure implies that the percentage improvement provided by Algorithm 1 over DMD is dependent on temporal frequency as opposed to noise covariance. Furthermore, p_ϵ increases as ω increases.

Figure 4(*b*) shows the DMD eigenvalues λ_i^{DMD} and OMD eigenvalues λ_i^{OMD} calculated for a fixed temporal frequency $\omega = 0.7$ and varying noise covariances $\sigma^2 \in [0.35^2, 1]$. For each noise covariance level, the pair of eigenvalues calculated by each of the algorithms is plotted. As noise covariance increases, both algorithms produce eigenvalues which are increasingly more stable (to the left of the figure) than the true eigenvalues $\lambda_{true} = 1 \pm 0.7i$. However, the OMD eigenvalue pairs are consistently closer to the true system eigenvalues than the DMD eigenvalues and hence provide a more accurate approximation of the relative growth rate error.

https://doi.org/10.1017/jfm.2013.426 Published online by Cambridge University Press

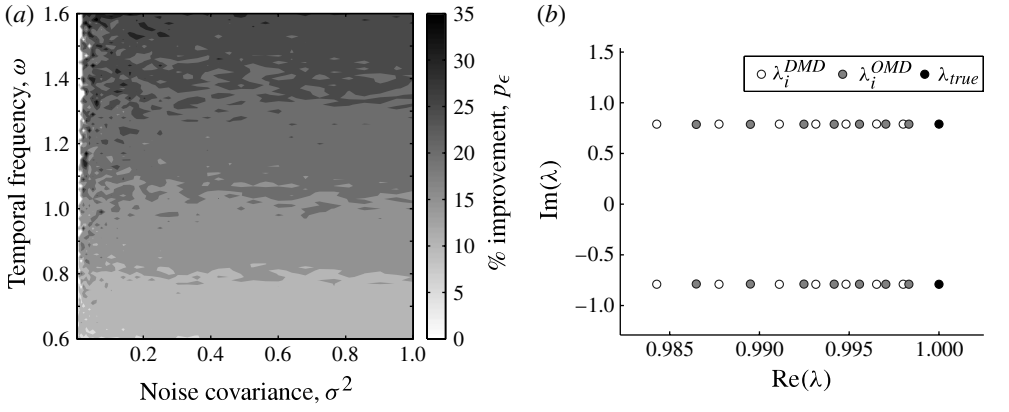


FIGURE 4. (*a*) Percentage improvement provided by Algorithm 1 to the DMD algorithm for the range $(\sigma^2, \omega) \in [0.05^2, 1] \times [0.6, 1.6]$. (*b*) DMD eigenvalues λ_i^{DMD} and OMD eigenvalues λ_i^{OMD} calculated for temporal frequency $\omega = 0.7$ and varying noise covariances. White shaded regions indicate both growth rate errors ϵ_{DMD}, ϵ_{OMD} are below tolerance $\epsilon = 10^{-4}$.

6. Analysis of the backward-facing step

A demonstration of the OMD algorithm on an experimental data set is now presented. The data set is of a low-speed turbulent boundary-layer flow over a backward-facing step, measured using two-dimensional time-resolved particle image velocimetry (PIV). The step, of height $h = 30$ mm, spans the full width of the wind tunnel and is downstream of a turbulent boundary layer of thickness $\delta = 44$ mm, with a free-stream velocity of 6 m s^{-1}. The PIV field of view is in the wall-normal plane parallel to the streamwise flow as schematically depicted in figure 5(*a*). The data is acquired at a frequency $F_s = 8000$ Hz for approximately 4 s, resulting in 31 606 images, from which 31 605 vector fields were calculated. The processing was done using a 16×16 pixel window with 50 % overlap, providing vector fields with a spatial resolution of approximately 1.1 mm. Figure 5(*b*) shows contours of the mean flow field, with streamlines overlaid to illustrate the size and shape of the recirculation region. The flow has a large recirculation region extending to approximately $x/h = 5$, and a smaller counter-rotating recirculation at the step face. Figure 5(*c*) shows an example of the streamwise velocity perturbation field $\boldsymbol{u}'(x, y)$, clearly depicting the turbulent shear layer at the edge of the separation region and large fluctuations in the vicinity of the downstream reattachment.

To analyse this data using either the DMD or OMD approach, a selection of the available data needs to be chosen. In the studies by Schmid (2010, 2011) the snapshots $\boldsymbol{u}_k$ are chosen as a sequence at regular intervals separated by Δt such that

$$\boldsymbol{u}_k^+ = \boldsymbol{u}_{k+1}. \tag{6.1}$$

In § 6.1 we follow this approach and apply DMD and OMD to such a sequential data set, so as to compare the algorithms in the setting in which DMD was developed. However, it should be noted that this is not the context in which OMD is intended to be applied. For this reason, in § 6.2, the OMD algorithm is also applied to snapshot pairs $(\boldsymbol{u}_k, \boldsymbol{u}_k^+)$ sampled at irregular time instances t_k.

There is no precise way of determining the best number of snapshots N and the temporal separation Δt of the snapshot pairs. Any appropriate selection is dependent

https://doi.org/10.1017/jfm.2013.426 Published online by Cambridge University Press

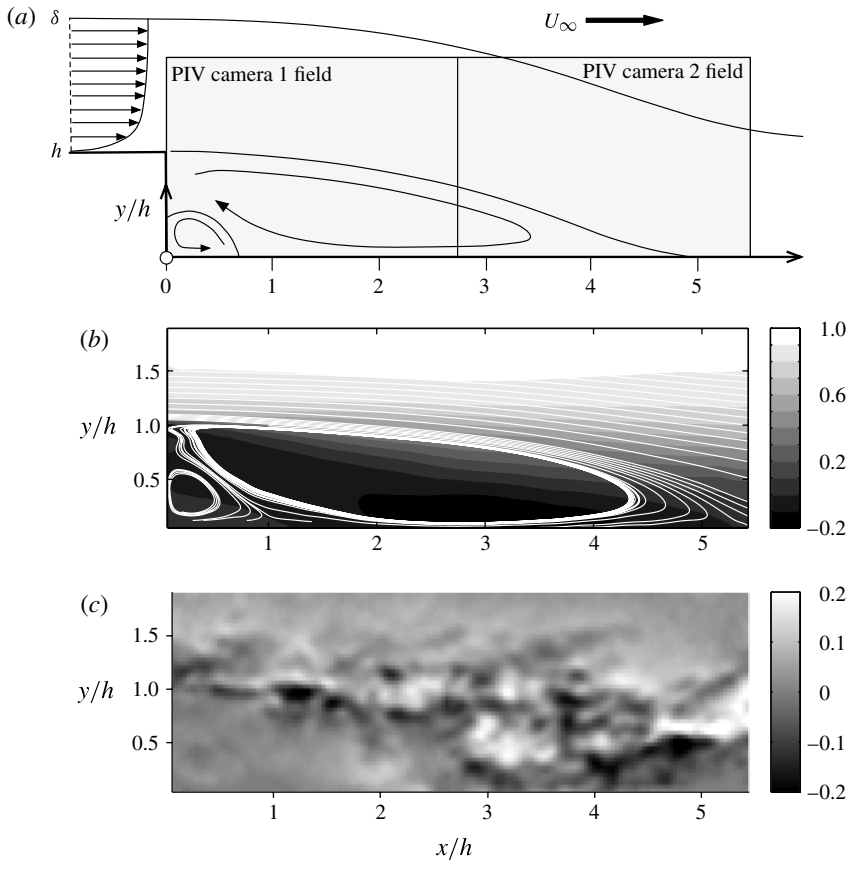


FIGURE 5. (*a*) A schematic representation of the PIV field of view and coordinate system; (*b*) contours of the mean streamwise velocity with selected mean streamlines; (*c*) an example of a PIV $\boldsymbol{u}'$ velocity field.

on the amount, type and format of the data and the dynamics to be modelled. Duke *et al.* (2012) calculated the relation between these parameters (among others) and the estimation error on the synthetic sinusoid (5.1). These results showed that, even for this simple waveform, the dependency of the relative growth rate error ϵ on the choice of method parameters is complex. They note in particular that error is sensitive to the data signal-to-noise ratio and the resolution of the data sampling.

Measurement noise is quantified by the magnitude of noise floor of the velocity power spectrum. Figure 6(*a*) shows the spectra for the present data at five different streamwise positions and a noise floor at approximately 2000 Hz is observed. This high-frequency measurement noise is over three orders of magnitude lower than the dominant low frequencies and, for all analyses performed in this section, is removed using a low-pass filter.

The appropriate choice of Δt needs to be made so that sufficient resolution is provided at the dominant frequencies modelled by the matrices $\tilde{\boldsymbol{S}}$ or $\boldsymbol{M}$. As shown in § 2.2, these matrices do not describe the evolution of the velocity field $\boldsymbol{u}_k \mapsto \boldsymbol{u}_k^+$, but rather that of the basis weights $\alpha_i \mapsto \alpha_i^+$. Furthermore, in § 2.4 it was shown that the DMD basis is the POD modes and that $\alpha_{i,DMD}$ are the POD weights. Since the POD

https://doi.org/10.1017/jfm.2013.426 Published online by Cambridge University Press

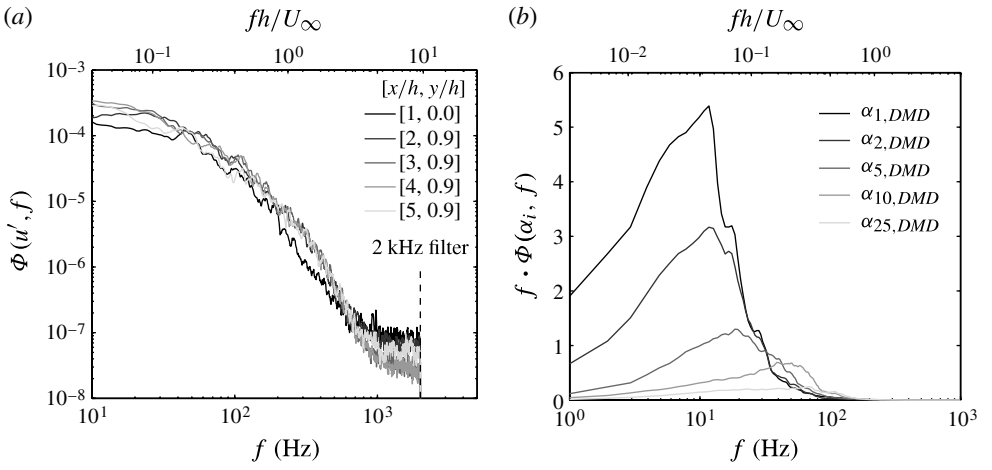


FIGURE 6. (*a*) The $\boldsymbol{u}'$ power spectral density of the flow at 5 streamwise locations with low-pass filter shown; (*b*) the premultiplied power spectra of the mode weights α_i.

basis is readily calculated for any data set, and is also a suitable initial condition for OMD optimization, inspecting the frequency content of $\alpha_{i,DMD}$ also serves as a useful guide to the choice of appropriate Δt for the OMD method.

Figure 6(*b*) is the premultiplied power spectra for the POD weights $\alpha_i(t)$ shown for $i = \{1, 2, 5, 10, 25\}$ over the full set of vector fields. The magnitude of the peak power of each mode varies, with the higher modes dominated by higher frequencies. However, all modes contain very little frequency content above 200 Hz and the most dominant frequencies are typically closer to 10 Hz. To achieve relative growth-rate errors of $\epsilon_{DMD} < 0.1\,\%$, Duke *et al.* (2012) recommend that the dominant wavelength should contain at least 40 samples. In addition, for a sequential data set, we require the total number of snapshots to span several full periods of the dominant wavelength. For the sequential data case studied in § 6.1 these criteria are satisfied by setting $N = 200$ and $\Delta t = 20/F_s$, which provide 5 full periods of data with frequency 10 Hz while keeping the computation within the capability of a desktop computer.

6.1. *Comparison between DMD and OMD for sequential data*

The individual modes of the $\boldsymbol{L}$ basis calculated using Algorithm 1 typically bear little resemblance to those of the POD basis $\boldsymbol{U}$ used in DMD. However, since both bases are composed of mutually orthogonal basis functions, each basis remains invariant under an orthogonal transformation $\boldsymbol{L} \mapsto \boldsymbol{LR}$. For the purposes of comparing the two, the $\boldsymbol{L}$ matrix can be transformed such that the modes are best aligned to the singular values of $\boldsymbol{B}$ in the same manner as a POD basis (Goulart *et al.* 2012). This is achieved using the singular value decomposition $\boldsymbol{L}^\top \boldsymbol{B} = \bar{\boldsymbol{U}}\bar{\Sigma}\bar{\boldsymbol{V}}^\top$ and setting $\boldsymbol{R} = \bar{\boldsymbol{U}}$. All of the following OMD results have been transformed in this way.

For a data set of the sequential form (6.1), the estimated mode weights at each sample point t_k

$$\hat{\alpha}^+_{i,DMD}(t_k) := \tilde{\boldsymbol{S}}\alpha_{i,DMD}(t_k); \quad \hat{\alpha}^+_{i,OMD}(t_k) := \boldsymbol{M}\alpha_{i,OMD}(t_k), \tag{6.2}$$

can be compared directly with the actual values

$$\alpha^+_{i,DMD}(t_k) = \alpha_{i,DMD}(t_{k+1}); \quad \alpha^+_{i,OMD}(t_k) = \alpha_{i,OMD}(t_{k+1}), \tag{6.3}$$

https://doi.org/10.1017/jfm.2013.426 Published online by Cambridge University Press

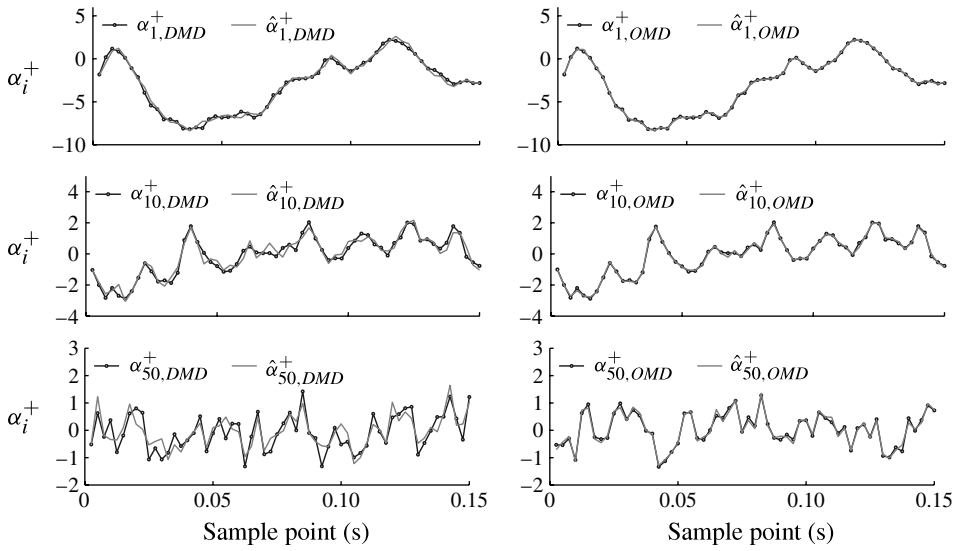


FIGURE 7. Comparison of the actual mode weights, α_i^+, with those estimated over a single time step, $\hat{\alpha}_i^+$, for both DMD and OMD analyses.

to demonstrate the single-point estimation capability of both methods. Figure 7 shows $\hat{\alpha}^+$ and α^+ for modes $i = \{1, 10, 50\}$ on a system of rank 100 using each method. The black markers indicate the sample points t_k with separation $\Delta t = 20/F_s$.

The actual weights (black lines) of the POD modes $\alpha_{i,DMD}^+$ and those of the transformed $\boldsymbol{L}$-basis $\alpha_{i,OMD}^+$ are similar at low modes, but are different at the higher modes, for example $i = 50$. This demonstrates that both methods use similar modes to describe the large structures, but have found different modes to represent the high frequencies. This extra freedom in mode shape selection allows OMD to produce dynamics which more accurately capture the evolution of the snapshot data.

In figure 7, it can be seen that, compared with DMD, the estimated weight sequence given by OMD more accurately models the true weights of the snapshot data when projected onto the identified low-order subspace. Figure 8(*a*) highlights this by showing the norm estimation error of each method for all 100 modes. The error of the OMD method is over four times lower than that of the DMD method across all modes. Figure 8(*b*) shows this translates into a lower estimation error of the system $\|\boldsymbol{A} - \boldsymbol{XB}\|$ as a whole. The difference in the error becomes larger as the system rank increases, meaning that the OMD algorithm performs proportionately better when the system has many modes. This is because, as shown in figure 7, OMD has the freedom to capture the high frequencies to a greater accuracy than DMD. This is a major advantage in systems for which the high-frequency (and often low-energy) modes play a crucial role in the flow dynamics (Ma *et al.* 2011).

We now consider the modes and eigenvalues produced by the OMD and DMD algorithms. Subsets of the eigenvalues of $\tilde{\boldsymbol{S}}$ and $\boldsymbol{M}$ are plotted against the unit circle in figure 9 for: (*a*) a rank-100; (*b*) a rank-150; and (*c*) a rank-200 mode approximation to the $N = 200$ mode sequential data ensemble. Figure 9(*a*) shows the eigenvalues corresponding to the rank-100 approximation analysed in figures 7 and 8. It can be seen that the OMD eigenvalues are concentrated in a narrower band than the DMD

https://doi.org/10.1017/jfm.2013.426 Published online by Cambridge University Press

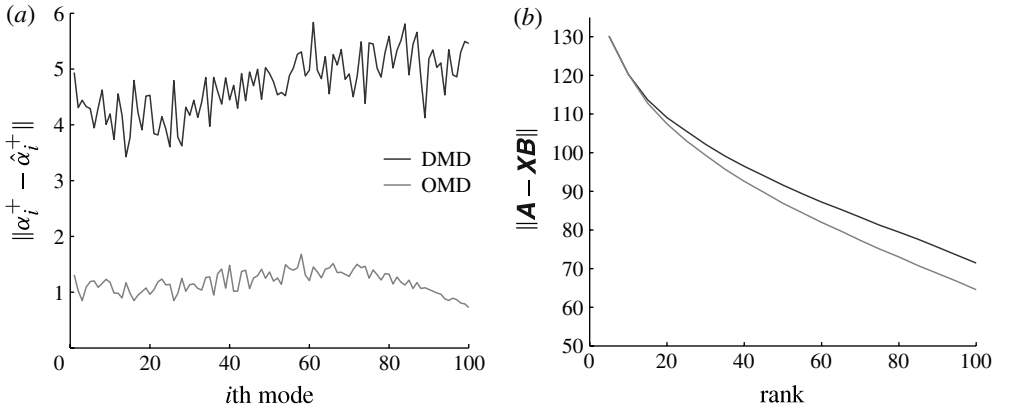


FIGURE 8. (*a*) The norm estimation error of α^+ using the DMD and OMD analyses, for each mode of a rank-100 system; (*b*) the norm system error for DMD and OMD analyses of systems with varying rank.

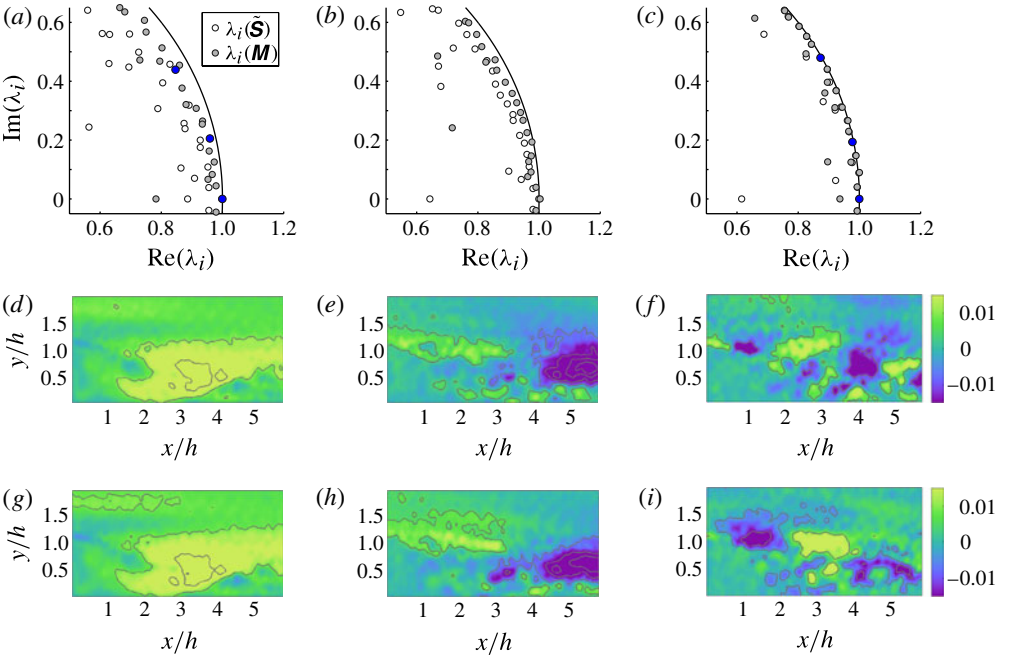


FIGURE 9. (Colour online) (*a–c*) Eigenvalues of $\tilde{\boldsymbol{S}}$ (DMD) and $\boldsymbol{M}$ (OMD) calculated using an ensemble of $N = 200$ sequential snapshots and with $r = 100, 150, 200$, respectively. In each case, the solid line is an arc of the unit circle. OMD modes corresponding to eigenvalues (highlighted in blue in the online version) in (*a*) are plotted as (*d–f*). DMD modes corresponding to eigenvalues (highlighted in blue in the online version) in (*c*) are plotted (*g–i*).

eigenvalues and are also closer to the unit circle, which corresponds to the right-shift trend observed for the sinusoidal waveform in figure 4(*b*). With increasing rank of approximation, the absolute difference between the OMD and DMD eigenvalues can

https://doi.org/10.1017/jfm.2013.426 Published online by Cambridge University Press

be seen to decrease in figure 9(*b,c*), although the shift trend is still clearly visible for the rank-150 approximation in figure 9(*b*).

In figure 9(*d–f*) the OMD modes corresponding to the eigenvalues (highlighted in blue in the online version) in figure 9(*a*) are shown. Despite the fact that a lower-rank system is used to generate them, it is interesting to note that they represent similar spatial structures to the fully converged DMD modes shown in figure 9(*g–i*), which correspond to the eigenvalues (highlighted in blue in the online version) in figure 9(*c*). The Strouhal numbers $St := fh/U_\infty$ of the highlighted OMD modes are $0, 0.452, 0.957$, respectively, and those of the DMD modes are $0, 0.391, 1.005$, respectively. We reserve comment on the physical interpretation of the mode shapes until § 6.2.

As discussed in § 3, the DMD modes can be viewed as approximations of the underlying Koopman modes of the system. The convergence of DMD and OMD modes for a full-rank ($r = 200,\ N = 200$) approximation implies that, for this example, OMD and DMD both provide similar approximations to the Koopman modes in this case. We restate, however, that it is not known which method produces the *best* approximation to the Koopman modes of a general nonlinear system. When a lower-order approximation is used, OMD is nonetheless able to produce mode shapes representing similar spatial structures to the fully converged DMD modes. We develop this idea in the following section by applying the OMD algorithm to an irregularly sampled data ensemble and show that coherent mode shapes can be created by using models of significantly lower rank than the dimension of the data ensemble.

6.2. *OMD modes and eigenvalues for irregularly sampled data*

The OMD algorithm is applied to a data ensemble $(\boldsymbol{u}_i, \boldsymbol{u}_i^+)_{i=1}^N$ containing $N = 800$ irregularly sampled snapshot pairs to create a rank $r = 16$ approximation. The fact that a only very low-order approximating system is searched for makes the problem computationally feasible. Furthermore, using a large number of snapshots helps account for any measurement noise present in the data ensemble. The OMD algorithm produces eigenvalues of $\boldsymbol{M}$ in an arc-like pattern symmetric about the real axis, as shown in figure 10(*a*). In comparison with the fully converged DMD and OMD eigenvalues in figure 9(*c*), which are distributed upon the entire unit circle and hence represent a wide frequency range, the arc of OMD eigenvalues in figure 10(*a*) corresponds to a set of relatively low-frequency modes. The OMD eigenvalues $\lambda_i^{OMD} = (\Delta t)^{-1} \log \lambda_i(\boldsymbol{M})$ are also plotted in figure 10(*b*).

The OMD mode shapes can be seen to separate into two subsets; low-frequency modes with lighter damping in figure 10(*c–e*) and more highly damped high-frequency modes in figure 10(*f–h*). The low-frequency modes are linked to the behaviour of the recirculation region, shown schematically in figure 5(*a*). Mode (*c*) is a near-persistent structure and resembles the modes 9(*d,g*) identified using the sequential data ensemble. Mode 10(*d*) has a region of recirculation near $y = 0$ in $2 \leqslant x/h \leqslant 4.5$. In addition, it contains a larger area of flow in the free-stream direction indicating coupling between the behaviour of the recirculation region and the shear layer. Mode 10(*e*) contains a large region of flow in the free-stream direction with a smaller region of reversed flow between $2 \leqslant x/h \leqslant 3$. This mode has similar spatial features to 9(*e,h*) although is has slightly lower frequency. Finally, modes 10(*f–h*) contain successive regions of low and high speeds in the shear layer that separates the recirculation region from the free stream. These modes represent the instabilities and the roll up of the shear layer. It is interesting to note that the high-frequency modes appear to be much more converged versions of the modes 9(*f,i*) identified from the sequential data ensemble. A possible explanation is that the low-order modelling capability of OMD allows the use of a

https://doi.org/10.1017/jfm.2013.426 Published online by Cambridge University Press

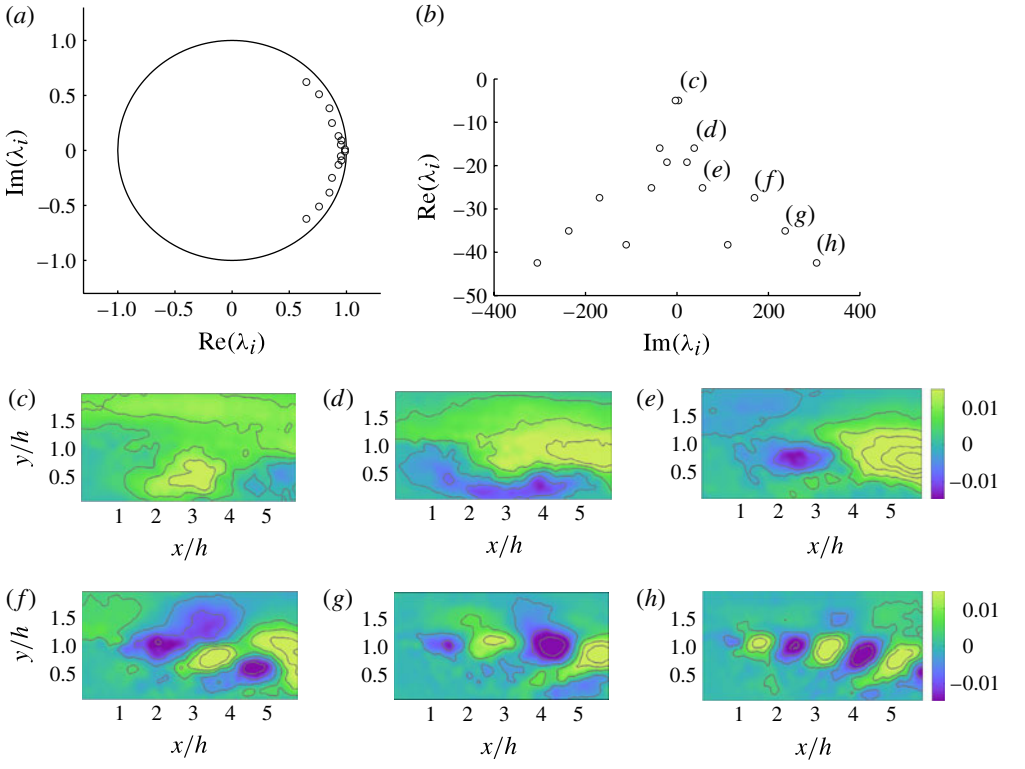


FIGURE 10. (Colour online) The OMD modes for turbulent flow over a backstep. A low-order model with $r = 16$ modes is calculated using $N = 800$ snapshot pairs. OMD eigenvalues shown in discrete (*a*) and continuous (*b*) time. Low-frequency modes (*c–e*) with Strouhal numbers $St = 0.017, 0.188, 0.279$ and high-frequency modes (*f–h*) with Strouhal numbers $St = 0.847, 1.1824, 1.527$.

large number of snapshots and enables a better extraction of coherent structures from the data ensemble.

7. Conclusions

A general method of approximating the dynamics of a high-dimensional nonlinear fluid system using a linear system of chosen rank has been presented. The system is first projected onto an orthogonal basis of chosen rank. The linear evolution of the flow is calculated on the low-rank basis, before projecting the result back to the original dimension. The choice of basis and the linear model are both variables in the optimization, in which the error $\|\boldsymbol{A} - \boldsymbol{XB}\|$ is minimized in the Frobenius norm.

It is shown that if the basis is chosen to be that of the system POD modes, and remains fixed during optimization, then the DMD solution results. The present method is therefore a generalization of the DMD algorithm.

The relation of OMD to Koopman modes is discussed and it is shown that OMD can be interpreted as providing a low-order approximation to the Koopman operator acting on the observable from which the system measurements result. Furthermore, it is shown that the OMD modes and eigenvalues approximate the Koopman modes an eigenvalues and that this approximation is a generalization of that provided by DMD.

https://doi.org/10.1017/jfm.2013.426 Published online by Cambridge University Press

However, we also highlight that it is not currently possible to prove mathematically which method (DMD, OMD or opt-DMD) provides the best approximation to the Koopman modes of a general nonlinear system.

The OMD method is tested on both synthetic and experimental data, and is shown to achieve a better approximation of the flow than DMD in terms of minimizing the system error norm. In the case of the synthetic example, OMD is shown to consistently provide a more accurate approximation of the true system eigenvalues than DMD in the presence of measurement noise. When applied to experimental data, the extra flexibility enjoyed by OMD in the selection of mode shapes allows high-frequency modes of the system to be more accurately identified. The high frequency contributions to the turbulent flow dynamics will therefore be better represented by OMD than if a POD basis were used. Therefore, this method is particularly appropriate for use in instances where such dynamics play a important role in the flow.

Acknowledgements

Financial support for this work from the European Union Seventh Framework Programme FP7/2007-2013 under the grant agreement number FP7-ICT-2009-4 248940 is greatly appreciated, as is the funding received from the EPSRC, through grant no. EP/F056206/1.

Appendix A

The following result shows that in the case of noise-free linear dynamics, the DMD matrix $\boldsymbol{S}$ exactly identifies the system eigenvalues.

THEOREM 1. *Suppose that snapshot data* $\{\boldsymbol{u}_1, \ldots, \boldsymbol{u}_{N+1}\}$ *satisfies purely linear dynamics* $\boldsymbol{u}_{i+1} = \boldsymbol{T}\boldsymbol{u}_i$, *for some matrix* $\boldsymbol{T} \in \mathbb{R}^{p\times p}$ *satisfying* $\operatorname{rank}(\boldsymbol{T}) \leqslant N$. *Let* $\boldsymbol{S}$ *be the minimizer of*

$$\min_{\boldsymbol{S}} \|\boldsymbol{A} - \boldsymbol{B}\boldsymbol{S}\|^2 \tag{A 1}$$

where $\boldsymbol{A} := [\boldsymbol{u}_2, \ldots, \boldsymbol{u}_{N+1}]$ *and* $\boldsymbol{B} := [\boldsymbol{u}_1, \ldots, \boldsymbol{u}_N]$. *Then* $\boldsymbol{T}$ *and* $\boldsymbol{S}$ *have the same non-zero eigenvalues.*

Proof. Let $m_T(x) := x^m + \alpha_{m-1}x^{m-1} + \cdots + \alpha_1 x + \alpha_0$ be the minimum polynomial of $\boldsymbol{T}$. Since $\operatorname{rank}(\boldsymbol{T}) \leqslant N$, it follows that $m \leqslant N$ and consequently,

$$\begin{aligned}\boldsymbol{u}_{N+1} = \boldsymbol{T}^N\boldsymbol{u}_1 = \boldsymbol{T}^{N-m}(\boldsymbol{T}^m\boldsymbol{u}_1) &= -\left[\alpha_{m-1}\boldsymbol{T}^{N-1}\boldsymbol{u}_1 + \cdots + \alpha_0\boldsymbol{T}^{N-m}\boldsymbol{u}_1\right] \\ &= -\left[\alpha_{m-1}\boldsymbol{u}_N + \cdots \alpha_0\boldsymbol{u}_{N-m+1}\right]. \end{aligned} \tag{A 2}$$

Hence, if $\boldsymbol{S}$ is the companion-form matrix

$$\begin{pmatrix} 0 & & & 0 \\ 1 & 0 & & \vdots \\ & 1 & & 0 \\ & & & -\alpha_0 \\ & & 0 & \vdots \\ & & 1 & -\alpha_{m-1} \end{pmatrix}, \tag{A 3}$$

https://doi.org/10.1017/jfm.2013.426 Published online by Cambridge University Press

then $\boldsymbol{A} = \boldsymbol{BS}$ and $\boldsymbol{S}$ is the minimizer of (A 1). It can now be shown that $\det(\boldsymbol{S} - \lambda \boldsymbol{I}) = \lambda^{n-m} m_T(\lambda)$, which implies that $\boldsymbol{S}$ and $\boldsymbol{T}$ have the same non-zero eigenvalues. □

In the remainder of this section we provide proofs of the results described in § 3.

A.1. *OMD, DMD, opt-DMD and the Koopman operator*

THEOREM 2. *Consider the data ensemble (3.6), generated in terms of a vector valued observable $g : Z \to \mathbb{C}^p$. Let $\boldsymbol{L} \in \mathbb{R}^{p\times r}$ be such that $\boldsymbol{L}^\top \boldsymbol{L} = \boldsymbol{I}$, suppose that $\boldsymbol{M} \in \mathbb{R}^{r\times r}$ is diagonalizable as $\boldsymbol{M} = \boldsymbol{T}\Lambda\boldsymbol{T}^{-1}$ and define $\mathscr{V} := \boldsymbol{B}^\top \boldsymbol{L}(\boldsymbol{L}^\top \boldsymbol{B}\boldsymbol{B}^\top \boldsymbol{L})^{-1}$. Then the observables Φ_i^L defined by (3.9) satisfy*

$$\left(\left(C\Phi_1^L\right)(z_1) \mid \cdots \mid \left(C\Phi_r^L\right)(z_1)\right) = (\boldsymbol{LT})\Lambda + \boldsymbol{L}(\boldsymbol{L}^\top \boldsymbol{A}\mathscr{V} - \boldsymbol{M})\boldsymbol{T}. \tag{A 4}$$

Proof. Denoting columnwise application of the Koopman operator by $C[\,\cdot\,]$, we begin with the relation $C[\boldsymbol{B}] = \boldsymbol{A}$. Multiplying on the right by $\mathscr{V}\boldsymbol{T}$ implies

$$C[\boldsymbol{B}\mathscr{V}\boldsymbol{T}] = \boldsymbol{A}\mathscr{V}\boldsymbol{T} = \boldsymbol{L}\boldsymbol{M}\boldsymbol{L}^\top \boldsymbol{B}\mathscr{V}\boldsymbol{T} + (\boldsymbol{A} - \boldsymbol{L}\boldsymbol{M}\boldsymbol{L}^\top \boldsymbol{B})\mathscr{V}\boldsymbol{T}. \tag{A 5}$$

Premultiply (A 5) by $\boldsymbol{L}\boldsymbol{L}^\top$ and use the identity $\boldsymbol{L}^\top \boldsymbol{B}\mathscr{V} = \boldsymbol{I}$ to obtain

$$C[\boldsymbol{L}\boldsymbol{L}^\top \boldsymbol{B}\mathscr{V}\boldsymbol{T}] = \boldsymbol{L}\boldsymbol{T}\Lambda + \boldsymbol{L}(\boldsymbol{L}^\top \boldsymbol{A}\mathscr{V} - \boldsymbol{M})\boldsymbol{T}. \tag{A 6}$$

The result follows since the columns of $C[\boldsymbol{L}\boldsymbol{L}^\top \boldsymbol{B}\mathscr{V}\boldsymbol{T}]$ are the vectors $(C\Phi_i^L)(z_1)$. □

LEMMA 1. *Suppose that $\Phi \in \mathscr{F}^p$ is a vector-valued eigenfunction of the Koopman operator C with eigenvalue λ. Then:*

(i) *there exists $\phi : Z \to \mathbb{C}$ such that $C\phi = \lambda\phi$;*

(ii) *if λ, when interpreted as an eigenvalue of a scalar-valued observable, is simple there exists $\boldsymbol{w} \in \mathbb{C}^p$ such that $\Phi = \boldsymbol{w}\phi$.*

Proof. (i) Let $\Phi(z) := \left(\phi^{(1)}(z), \ldots, \phi^{(p)}(z)\right)^\top$ denote the p scalar-valued components of the observable Φ. Then since $(C\Phi)(z) = \lambda\Phi(z)$, it follows that $(C\phi^{(i)})(z) = \lambda\phi^{(i)}(z)$ for each i. Since Φ is an eigenfunction, at least one component is non-zero and hence λ is an eigenvalue of a scalar-valued observable.

(ii) If λ is simple, there exist scalars $w_i \in \mathbb{C}$ such that $\phi^{(i)} = w_i\phi$, for each i. Hence, $\Phi = \boldsymbol{w}\phi$ for $\boldsymbol{w} := (w_1, \ldots, w_p)^\top \in \mathbb{C}^p$. □

THEOREM 3. *Suppose that $\{\boldsymbol{u}_1, \ldots, \boldsymbol{u}_N\}$ is a sequential data ensemble containing snapshots taken at a fixed time step Δt apart. Then the optimal value of the minimization problem (3.14) is equal to the optimal value of (3.15).*

Proof. Suppose first that $\boldsymbol{L}$, $\boldsymbol{M}$, ξ_1 are feasible decision variables for (3.15). Since $\boldsymbol{M}$ is diagonalizable, there exists invertible $\boldsymbol{U} \in \mathbb{R}^{r\times r}$ and $\Lambda = \operatorname{diag}\begin{pmatrix}\lambda_1 & \ldots & \lambda_r\end{pmatrix}$ such that $\boldsymbol{M} = \boldsymbol{U}\Lambda\boldsymbol{U}^{-1}$. Since $\xi_1 \in \operatorname{Im}(\boldsymbol{L}) = \operatorname{Im}(\boldsymbol{LU})$, there exists $\sigma_i \in \mathbb{R}$ such that

$$\xi_1 = \sum_{i=1}^{r} \sigma_i (\boldsymbol{LU})_i = \boldsymbol{LU}\Sigma\boldsymbol{1} \tag{A 7}$$

where $\Sigma = \operatorname{diag}\begin{pmatrix}\sigma_1 & \ldots & \sigma_r\end{pmatrix}$, $\boldsymbol{1} = \begin{pmatrix}1 & \ldots & 1\end{pmatrix}^\top \in \mathbb{R}^r$ and $(\boldsymbol{LU})_i$ denotes the ith column of $\boldsymbol{LU}$. Now, let $\boldsymbol{V} := \boldsymbol{LU}\Sigma \in \mathbb{R}^{p\times r}$ and $\boldsymbol{T} \in \mathbb{R}^{r\times N}$ be the Vandermonde matrix

https://doi.org/10.1017/jfm.2013.426 Published online by Cambridge University Press

defined in terms of the eigenvalues of Λ. Then

$$\begin{aligned}\sum_{i=1}^{N} \|\boldsymbol{u}_i - (\boldsymbol{LML}^\top)^{i-1}\xi_1\|_2^2 &= \sum_{i=1}^{N} \|\boldsymbol{u}_i - (\boldsymbol{LU}\Lambda^{i-1}\boldsymbol{U}^{-1}\boldsymbol{L}^\top)\xi_1\|_2^2 \\ \text{(by (A 3))} &= \sum_{i=1}^{N} \|\boldsymbol{u}_i - \boldsymbol{LU}\Lambda^{i-1}\Sigma\mathbf{1}\|_2^2 \\ &= \sum_{i=1}^{N} \|\boldsymbol{u}_i - (\boldsymbol{LU}\Sigma)\lambda^{(i-1)}\|_2^2 \\ &= \|\boldsymbol{B} - \boldsymbol{VT}\|^2 \end{aligned} \tag{A 8}$$

where $\lambda^{(i)} := \begin{pmatrix}\lambda_1^i & \dots & \lambda_r^i\end{pmatrix}^\top$. Hence, the optimal value of (3.14) is less than the optimal value of (3.15).

Conversely, suppose that $(\boldsymbol{V}, \boldsymbol{T})$ are feasible decision variables for (3.14) with $\boldsymbol{T}$ defined in terms of eigenvalues $\lambda_1, \dots, \lambda_r$. Let $\boldsymbol{V} = \boldsymbol{LZ}$ be a reduced QR-decomposition of $\boldsymbol{V}$, $\boldsymbol{M} := \boldsymbol{Z}\Lambda\boldsymbol{Z}^{-1}$ and $\xi_1 := \sum_{i=1}^{N} V_i \in \mathrm{Im}(\boldsymbol{L})$. Then, similar to above, it can be shown that (A 8) holds. Hence, the optimal value of (3.14) is less than the optimal value of (3.15), which completes the proof. □

Appendix B. An example

We present a simple illustrative example for which OMD provides a superior estimate of the system dynamics relative to that produced via DMD when used to reduce the system order. Consider the following system:

$$\boldsymbol{x}^+ = \begin{pmatrix}\lambda^{true} & 0 \\ 0 & 0\end{pmatrix}\boldsymbol{x} + \boldsymbol{w}, \tag{B 1}$$

where $\lambda^{true} = 0.5$ and $\boldsymbol{w}$ is a normally distributed random variable with zero mean and variance $\mathbb{E}(\boldsymbol{ww}^\top) = diag(1, 10)$. The initial state is $\boldsymbol{x} = (1; 0)$ and the system is simulated for $N = 1000$ time steps.

Assume that we want a rank-one approximation for the preceding system. Using the DMD method, we obtain

$$\begin{aligned}\boldsymbol{L}^*_{DMD} &= \begin{pmatrix}-0.002 \\ 0.999\end{pmatrix}, \quad \boldsymbol{M}^*_{DMD} = 0.028, \\ (\boldsymbol{LML}^\top)^*_{DMD} &= \begin{pmatrix}+1.2 \times 10^{-7} & -5.8 \times 10^{-5} \\ -5.8 \times 10^{-5} & +0.028\end{pmatrix},\end{aligned} \tag{B 2}$$

but with OMD,

$$\begin{aligned}\boldsymbol{L}^*_{OMD} &= \begin{pmatrix}0.999 \\ 0.005\end{pmatrix}, \quad \boldsymbol{M}^*_{OMD} = 0.509, \\ (\boldsymbol{LML}^\top)^*_{OMD} &= \begin{pmatrix}+0.509 & +2.5 \times 10^{-3} \\ +2.5 \times 10^{-3} & +3.6 \times 10^{-5}\end{pmatrix}.\end{aligned} \tag{B 3}$$

Note that the difference in the performance metric $\|\boldsymbol{A} - \boldsymbol{XB}\|$ is relatively small due to the process noise in the system; $\|\boldsymbol{A} - (\boldsymbol{LML}^\top)^*_{OMD}\boldsymbol{B}\| = 105.9$ for OMD, compared

https://doi.org/10.1017/jfm.2013.426 Published online by Cambridge University Press

to $\|A - (\boldsymbol{L}\boldsymbol{M}\boldsymbol{L}^{\top})^{*}_{DMD}\boldsymbol{B}\| = 107.5$ for DMD. A more revealing performance metric is the matrix induced 2-norm (i.e. the spectral norm) error $\left\|(\boldsymbol{L}\boldsymbol{M}\boldsymbol{L}^{\top})^{*} - diag(\lambda^{true}, 0)\right\|_2$. The results are

$$\left\|(\boldsymbol{L}\boldsymbol{M}\boldsymbol{L}^{\top})^{*}_{DMD} - diag(\lambda^{true}, 0)\right\|_2 = 0.5 \tag{B 4a}$$

$$\left\|(\boldsymbol{L}\boldsymbol{M}\boldsymbol{L}^{\top})^{*}_{OMD} - diag(\lambda^{true}, 0)\right\|_2 = 0.009 \tag{B 4b}$$

showing that OMD significantly outperforms DMD in identifying the underlying system.

Appendix C

The partial derivative $g_{\boldsymbol{L}} := (\partial g/\partial \boldsymbol{L})(\boldsymbol{L})$ of the objective function g appearing in (4.2) can be shown (Goulart *et al.* 2012) to be equal to

$$\begin{aligned} g_{\boldsymbol{L}} = &-2\mathscr{B}\boldsymbol{L}(\boldsymbol{L}^{\top}\mathscr{B}\boldsymbol{L})^{-1}(\boldsymbol{L}^{\top}\mathscr{A}^{\top}\boldsymbol{L})(\boldsymbol{L}^{\top}\mathscr{A}\boldsymbol{L})(\boldsymbol{L}^{\top}\mathscr{B}L)^{-1} \\ &+2\left[\mathscr{A}\boldsymbol{L}(\boldsymbol{L}^{\top}\mathscr{B}\boldsymbol{L})^{-1}(\boldsymbol{L}^{\top}\mathscr{A}^{\top}\boldsymbol{L}) + \mathscr{A}^{\top}\boldsymbol{L}(\boldsymbol{L}^{\top}\mathscr{A}\boldsymbol{L})(\boldsymbol{L}^{\top}\mathscr{B}\boldsymbol{L})^{-1}\right], \end{aligned} \tag{C 1}$$

where $\mathscr{A} := \boldsymbol{A}\boldsymbol{B}^{\top}$ and $\mathscr{B} := \boldsymbol{B}\boldsymbol{B}^{\top}$.

With respect to Algorithm 1 the conjugate-gradient correction term Δ_{k+1} is given by

$$\Delta_{k+1} := \frac{\langle \boldsymbol{G}_{k+1} - \tau(\boldsymbol{G}_k), \boldsymbol{G}_{k+1}\rangle}{\|\boldsymbol{G}_{k+1}\|^2}\tau(\boldsymbol{H}_k), \tag{C 2}$$

where

$$\tau(\boldsymbol{G}_k) := \boldsymbol{G}_k - (\boldsymbol{L}_k\boldsymbol{V}\sin(\Sigma t_k) + \boldsymbol{U}(\boldsymbol{I} - \cos(\Sigma t_k)))\boldsymbol{U}^{\top}\boldsymbol{G}_k \tag{C 3}$$

$$\tau(\boldsymbol{H}_k) := (-\boldsymbol{L}_k\boldsymbol{V}\sin(\Sigma t_k) + \boldsymbol{U}\cos(\Sigma t_k))\Sigma\boldsymbol{V}^{\top} \tag{C 4}$$

and $\boldsymbol{H}_k = \boldsymbol{U}\Sigma\boldsymbol{V}^{\top}$ is a singular value decomposition of $\boldsymbol{H}_k$. The constant $t_k \in [0, 1]$ is the minimizer in Algorithm 1, step 4, at the kth iterate.

Appendix D

In the case of a large data ensemble (N large), the following procedure can be applied to reduce the dimension of the optimization problem which must be solved to calculate the OMD eigenvalues and modes.

Suppose that we select a matrix $\boldsymbol{\Gamma} \in \mathbb{R}^{p\times s}$ satisfying $\boldsymbol{\Gamma}^{\top}\boldsymbol{\Gamma} = \boldsymbol{I}$, $\mathrm{Im}(\boldsymbol{\Gamma}) \subseteq \mathrm{Im}(\boldsymbol{B})$ and $s \leqslant N$, e.g. by setting $\boldsymbol{\Gamma}$ equal to the first s right singular vectors of $\boldsymbol{B}$. One can then constrain the basis vectors $\boldsymbol{L}$ to those in the form

$$\boldsymbol{L} = \boldsymbol{\Gamma}Z, \quad \boldsymbol{Z} \in \mathbb{R}^{s\times r}, \quad \boldsymbol{Z}^{\top}\boldsymbol{Z} = \boldsymbol{I}. \tag{D 1}$$

Such a constraint amounts to requiring that the columns of $\boldsymbol{L}$ are themselves restricted to some subspace of $\mathrm{Im}(\boldsymbol{B})$. Using this additional constraint, the objective function in (2.11) can be rewritten as

$$\left\|\boldsymbol{A} - \boldsymbol{L}\boldsymbol{M}\boldsymbol{L}^{\top}\boldsymbol{B}\right\|^2 = \left\|\boldsymbol{A} - \boldsymbol{\Gamma}\boldsymbol{Z}\boldsymbol{M}\boldsymbol{Z}^{\top}\boldsymbol{\Gamma}^{\top}\boldsymbol{B}\right\|^2. \tag{D 2}$$

Since this objective is invariant under a unitary transformation, we can left-multiply both terms by the transpose of $\boldsymbol{\Gamma}$ augmented with its orthogonal complement $\boldsymbol{\Gamma}_{\perp}$ to obtain

$$\left\|\boldsymbol{A} - \boldsymbol{\Gamma}\boldsymbol{Z}\boldsymbol{M}\boldsymbol{Z}^{\top}\boldsymbol{\Gamma}^{\top}\boldsymbol{B}\right\|^2 = \left\|\boldsymbol{\Gamma}^{\top}\boldsymbol{A} - \boldsymbol{Z}\boldsymbol{M}\boldsymbol{Z}^{\top}\boldsymbol{\Gamma}^{\top}\boldsymbol{B}\right\|^2 + \left\|\boldsymbol{\Gamma}_{\perp}^{\top}\boldsymbol{A}\right\|^2. \tag{D 3}$$

https://doi.org/10.1017/jfm.2013.426 Published online by Cambridge University Press

It is clear that the approximation error introduced by this constraint on $\boldsymbol{L}$ will be no larger than $\|\boldsymbol{\Gamma}_\perp^\top \boldsymbol{A}\|^2$. This term will be small, for example, in cases where the images of $\boldsymbol{A}$ and $\boldsymbol{B}$ are nearly coincident and $\boldsymbol{\Gamma}$ spans their dominant left singular vectors.

If we then define $\tilde{\boldsymbol{A}} \in \mathbb{R}^{s\times N}$ as $\tilde{\boldsymbol{A}} := \boldsymbol{\Gamma}^\top \boldsymbol{A}$ and $\tilde{\boldsymbol{B}} \in \mathbb{R}^{s\times N}$ as $\tilde{\boldsymbol{B}} := \boldsymbol{\Gamma}^\top \boldsymbol{B}$, then we arrive at the new optimization problem

$$\begin{aligned} \min \quad & \|\tilde{\boldsymbol{A}} - \boldsymbol{Z}\boldsymbol{M}\boldsymbol{Z}^\top \tilde{\boldsymbol{B}}\|^2 \\ \text{s.t.} \quad & \boldsymbol{Z}^\top \boldsymbol{Z} = \boldsymbol{I} \\ & \boldsymbol{M} \in \mathbb{R}^{r\times r}, \ \ \boldsymbol{Z} \in \mathbb{R}^{s\times r}. \end{aligned} \tag{D 4}$$

This is exactly the same form as the original problem (2.11), meaning that Algorithm 1 may be applied to provide a solution. However, (D 4) is a smaller optimization problem than (2.11) and may therefore be solved more efficiently.

REFERENCES

ABSIL, P. A., MAHONY, R. & SEPULCHRE, R. 2008 *Optimization Algorithms on Matrix Manifolds*. Princeton University Press.

BAGHERI, S. 2013 Koopman-mode decomposition of the cylinder wake. *J. Fluid Mech.* **726**, 596–623.

BONNET, J. P., COLE, D. R., DELVILLE, J., GLAUSER, M. N. & UKEILEY, L. S. 1994 Stochastic estimation and proper orthogonal decomposition: complementary techniques for identifying structure. *Exp. Fluids* **17**, 307–314.

BUDIŠIĆ, M., MOHR, R. & MEZIĆ, I. 2012 Applied Koopmanism. *Chaos: An Interdisciplinary Journal of Nonlinear Science* **22** (4), 047510.

CHEN, K. K., TU, J. H. & ROWLEY, C. W. 2012 Variants of dynamic mode decomposition: boundary condition, Koopman, and Fourier analyses. *J. Nonlinear Sci.* **22** (6), 887–915.

DUKE, D., SORIA, J. & HONNERY, D. 2012 An error analysis of the dynamic mode decomposition. *Exp. Fluids* **52** (2), 529–542.

EDELMAN, A., ARIAS, T. A. & SMITH, S. T. 1998 The geometry of algorithms with orthogonality constraints. *SIAM J. Matrix Anal. Appl.* **20** (2), 303–353.

GOULART, P. J., WYNN, A. & PEARSON, D. 2012 Optimal mode decomposition for high dimensional systems. In *51st IEEE Conference on Decision and Control. Maui, Hawaii*. Available at: http://control.ee.ethz.ch/~goularpa/.

ILAK, M. & ROWLEY, C. W. 2008 Modelling of transitional channel flow using balanced proper orthogonal decomposition. *Phys. Fluids* **20** (034103).

JUANG, J.-N. & PAPPA, R. S. 1985 An eigensystem realization algorithm for modal parameter identification and model reduction. *J. Guid. Control Dyn.* **8** (5), 20–27.

LUMLEY, J. L. 1970 *Stochastic Tools in Turbulence*. Academic.

MA, Z., AHUJA, S. & ROWLEY, C. W. 2011 Reduced-order models for control of fluids using the eigensystem realization algorithm. *Theor. Comp. Fluid Dyn.* **25**, 233–247.

MEZIĆ, I. 2013 Analysis of fluid flows via spectral properties of the Koopman operator. *Annu. Rev. Fluid Mech.* **45** (1), 357–378.

NOACK, B. R., AFANASIEV, K., MORZYNSKI, M., TADMOR, G. & THIELE, F. 2003 A hierarchy of low-dimensional models for the transient and post-transient cylinder wake. *J. Fluid Mech.* **497**, 335–363.

PASTOOR, M., HENNING, L., NOACK, B. R., KING, R. & TADMOR, G. 2008 Feeback shear layer control for bluff body drag reduction. *J. Fluid Mech.* **608**, 161–196.

ROWLEY, C. W. 2005 Model reduction for fluids, using balanced proper orthogonal decomposition. *Intl J. Bifurcation Chaos* **15** (3), 997–1013.

ROWLEY, C. W., MEZIĆ, I., BAGHERI, S., SCHLATTER, P. & HENNINGSON, D. S. 2009 Spectral analysis of nonlinear flows. *J. Fluid Mech.* **641**, 85–113.

SCHMID, P. J. 2010 Dynamic mode decomposition of numerical and experimental data. *J. Fluid Mech.* **656**, 5–28.

https://doi.org/10.1017/jfm.2013.426 Published online by Cambridge University Press

SCHMID, P. J. 2011 Application of the dynamic mode decomposition to experimental data. *Exp. Fluids* **50** (4), 1123–1130.

SIROVICH, L. 1987 Turbulence and the dynamics of coherent structures. *Q. Appl. Maths* **45**, 561–590.

TADMOR, G., GONZALEZ, J., LEHMANN, O., NOACK, B. R., MORZYŃSKI, M. & STANKIEWICZ, W. 2007 Shift modes and transient dynamics in low order, design oriented Galerkin models. In *45th AIAA Aerospace Sciences Meeting and Exhibit, 8–11 January*. *AIAA Paper* 2007-0111.

https://doi.org/10.1017/jfm.2013.426 Published online by Cambridge University Press